BACKSCATTER CHARACTERISTICS OF THE WINTER SEA ICE COVER IN THE BEAUFORT

Ronald Kwok and Glenn F. Cunningham

Jet Propulsion Laboratory
California Institute of Technology
4800 Oak Grove Drive
Pasadena, CA 91109

Submitted to *JGR Oceans*

May 13, 1993

Corresponding author:

Dr. Ronald Kwok
Jet Propulsion Laboratory
California Institute of Technology
MS 300-235
4800 Oak Grove Drive
Pasadena, CA 91109

BACKSCATTER CHARACTERISTICS OF THE WINTER SEA ICE COVER IN THE BEAUFORT

Ronald Kwok and Glenn F. Cunningham
Jet Propulsion Laboratory
California Institute of Technology
Pasadena, CA 91109

Abstract

The microwave backscatter statistics of the sea ice cover in the winter Beaufort Sea were characterized using C-band Synthetic Aperture Radar (SAR) data collected by ERS-1. Sea ice backscatter signatures were sampled from SAR image data collected during the winter of 1991/92 and winter of 1992/93. The spatial and temporal variabilities of the backscatter signatures of different ice types are discussed. The results show considerable seasonal stability of the backscatter signature of multi-year ice as well as first-year ice. Small amplitude regional variations of the multi-year ice backscatter can be observed. Consistent contrast between multiyear ice and first-year ice is maintained throughout the season. The highest radiometric variability is observed in sea ice in leads. Based on these observations, the backscatter from the principal ice types (multiyear and first-year) are consistent with scatterometer observations and can be easily identified under winter conditions. Correlations of the regional variations of multiyear ice signatures to physical processes are suggested.

1 Introduction

The spatial and temporal coverage of the ERS-1 SAR provide an opportunity to systematically monitor the regional and seasonal behavior of the backscatter signatures of sea ice from a spaceborne sensor. The effective retrieval of ice type information from radar data is dependent on the uniqueness of these radar signatures as well as their quantitative description. Numerous studies [e.g. *Ulaby et al.*, 1986; *Onstott et al.*, 1979, 1982; *Kim et al.*, 1985; *Livingstone and Drinkwater*, 1991; *Gray et al.*, 1982] during recent years have investigated the dependence of sea ice backscatter on frequency, incidence angle, and polarization. These ice signatures also vary significantly with seasonal temperature variations [*Onstott and Gogineni*, 1985; *Onstott et al.*, 1987; *Holt and Digby*, 1985; *Livingstone et al.*, 1987A; *Carsey*, 1985; *Cavalieri et al.*, 1990; *Livingstone et al.*, 1987B]. Several recent studies have compared theoretical scattering models based on ice properties to the observed radar ice signatures [*Drinkwater et al.*, 1991; *Winebrenner et al.*, 1989; *Drinkwater*, 1989; *Kim et al.*, 1985]. These studies include in-situ, laboratory, and aircraft measurements with some coordinated ground support. They have demonstrated that sea ice types have well-defined radar scattering signatures under certain environmental conditions. Indeed, algorithms [*Lyden et al.*, 1984; *Wackerman et al.*, 1988; *Shokr*, 1992; *Kwok et al.*, 1992] have been developed to utilize these frequency and polarization diverse measurements for identification of ice types in remote sensing data. While these studies are useful for obtaining fundamental knowledge about the scattering properties of sea ice, the areal coverage has usually been very sparse and the observation periods too limited to permit good spatial and temporal characterizations of the scattering signature of the sea ice cover. The regional dependence of ice signatures derived from spaceborne radar data is not well-known.

The purpose of this work is to provide a more extended study of the C-band VV backscatter signature of sea ice in the winter Beaufort Sea using data collected by the ERS-1 SAR. The spatial and temporal characterization of ice signatures also enables the evaluation of the statistical variability of sea ice backscatter. Here, we use the seasonal descriptors suggested by *Livingstone et al.* [1987] and restrict our sampling to only *winter* conditions when typically there is a dry snow pack overlying dry cold ice with air temperatures that are less than -10°C. In this study, we characterize the microwave signature of sea ice in the Beaufort Sea winter of 1991/92 and winter of 1992/93. Such characterizations are important when a unique set of signatures for each ice type are required for the eventual extraction of information from satellite data.

Under cold dry winter conditions, it has been observed that there is significant contrast between multiyear ice and first-year ice when the probing frequency is C-band or higher. The significance of particular sea-ice characteristics and their effects on microwave backscatter was summarized in *Winebrenner et al.* [1989]. The relatively higher contribution of the multiyear ice volume, compared to the ice surface, to the scattering process is the generally accepted physical explanation for the observed contrast in backscatter. In sea ice, as in most natural media, electromagnetic scattering takes place from inhomogeneities within the volume of the medium, from irregular surfaces bounding the medium, or from both. The fundamental difference between backscatter from first-year and multiyear ice is the higher salinity of the former. The superimposed dry snow layer does not significantly affect the observed backscatter at C-band [*Kim et al.*, 1985]. For a given surface roughness, then, the contribution to the scattering cross-section from these inhomogeneities (air bubbles, brine pockets) in the multiyear ice is much higher due to the low salinity in the ice layer. The signature dynamics of younger and thinner ice types, however, are more complex and less well-defined from a uniqueness point of view. The characterization of these signatures,

which is not readily done in ERS-1 SAR imagery, is more involved and is not treated in this study.

The calibration of the ERS-1 SAR is reviewed in section 2. We describe our approach to spatial and temporal sampling of the sea ice signatures in section 3. The multiyear, first-year and lead ice type signature records are summarized in sections 4 and 5. Summary remarks are provided in the last section.

2 Data Calibration and Characteristics

The data used in this study were collected by the ERS-1 Synthetic Aperture Radar. The sensor is a C-band (5.3GHz) radar operated with vertical transmit and receive polarizations at a look angle of 20°. Within the antenna beam, which illuminates a swath of approximately 100km in width, the incidence angles on the ground vary from 19° at near range to almost 26° at far range. The image data used in this study were received and processed at the Alaska SAR Facility (ASF) in Fairbanks, Alaska. Each image frame covers an area of approximately 100km by 100km. The SAR processor at ASF produces full-resolution ground plane data which is sampled at 12.5m. The data type used in this study is a lower resolution image product created by increasing the sample spacing to 100m by the averaging of 8x8 full-resolution pixel samples. Ancillary data is provided with each image frame for calibration and conversion of the 8-bit digital data into normalized backscatter cross-sections.

Calibration of the radar is measured in an absolute and relative sense. The absolute calibration accuracy metric quantifies the uncertainty of a measured normalized backscatter cross-section (σ_o) measurement relative to the actual σ_o of a distributed target. Typically, this appears as a bias when an identical target from two image

frames (imaged at different times) are compared. The in-scene variance of a target known to have uniform backscatter cross-section is measured by the relative calibration accuracy. Relative calibration is usually better than absolute calibration and is easily maintainable especially if the radar sensor is stable. The data products used in this study have expected absolute and relative accuracies of 2dB and 1dB, respectively [*Fatland and Freeman*, 1991]. The noise equivalent σ_o of the ERS-1 radar data is at approximately -24dB, which means that the backscatter power from a distributed target with a σ_o of -24dB is equivalent to the noise power of the sensor. The detectability of such backscatter targets is therefore limited by this quantity. We note here that low backscatter sea ice (e.g. grease ice) in the incidence angle range of ERS-1 could be less than -30dB and is therefore in theory radiometrically undetectable within the dynamic range of the data. The above factors provide the limits to the observations made here. Because of the expected range of backscatter first-year and multiyear ice, the observations of their temporal and regional backscatter characteristics should not be significantly affected by these factors.

3 Data Analysis Approach

The geographic bounds of the area studied are shown in Figure 1. A first dataset was obtained from data collected during the 3-day repeat cycles of the ERS-1 *commissioning* and *ice* phases. There were four descending SAR tracks which covered a region bounded on the south by the Alaskan and Canadian coasts, on the east by Banks Island and Prince Patrick Island, and on the west by a line running from 70°N, 160°W to approximately 83°N, 135°W. The *commissioning* phase lasted from August 6 through December 9, 1991, while the *ice* phase lasted from December 28, 1991 through April 2, 1992 after an 18 day orbit adjustment period between phases.

This first dataset provided us with a temporal record of ice signatures spanning six winter months from October 1991 through March 1992. The second smaller dataset was obtained from data collected from similar descending tracks during the *multi-disciplinary* phase (35-day repeat) in the months of November and December of 1992. These two datasets provide us with a comparison of winter ice signatures of the sea ice cover for two consecutive winters. The data presented in the following sections are labelled and organized by these four tracks, designated hereafter by the land boundaries they intersect: *ptb* - Point Barrow; *prb* - Prudhoe Bay; *alc* - Alaskan/Canadian border; and *ppi* - Prince Patrick Island.

Samples for signature characterization were extracted from images when the air temperature was below -10°C at the time of acquisition. Under these winter conditions when the typical observed scattering configuration is cold dry snow over an ice layer, the temperature modulation of the backscatter should be small. This ensures that the collected statistics are not contaminated by mixtures of ice and ice with surface melt. Figure 2 shows the region-wide air temperature record over the Beaufort Sea during the period of interest. This air temperature time series was derived from gridded (2.5° latitude by 5°longitude grid) 12-hourly NMC 1000-mb air temperature analyses. While these temperatures may not represent the actual physical surface air temperature due to uncertainty in the NMC analyses (typically the temperature fields are biased due to difficulty in modelling the inversion layer), they are nevertheless indicators of the winter conditions predicated in this study. The data show that the region-wide average temperature stayed below -10°C starting around DOY(Day of Year) -52 or November 9, 1991. Temperatures at actual SAR image center times and locations show that all but 5 images were acquired when the temperature was below -10°C.

Due to the large number of SAR image products which were available over the four

tracks, a spatial and temporal sampling strategy was utilized and is described below. The tracks were sampled every 12-days in the first dataset. In the second dataset, the tracks were sampled once in November and December. Table 1 summarizes the temporal and spatial coverage of the two datasets. The DOY and number of images sampled are given for each orbit. A gap in the table indicates that images for that time had not been processed by ASF at the time of this study. In all, more than 600 images were used in this study.

Figure 3 shows a typical ERS-1 sea ice image from the winter Beaufort. The higher backscatter multiyear ice can easily be discriminated from the other ice types. Upon closer examination, at least 2-3 other ice types can be identified (using their backscatter intensities). In this study, sample windows were visually classified as one of five ice types from the perennial ice zone (PIZ) and the seasonal ice zone (SIZ). The rationale for this classification is the relative ease with which samples can be visually identified. It should be noted here that due to the disparity between the resolution of typical land-based scatterometer and spaceborne SAR observations, it is expected that SAR image backscatter observations are modulated to a higher degree by mixtures of ice types compared with scatterometer samples. It is expected that observations at the larger scale could be biased or have larger variance in backscatter than the pure ice type. The image statistics were collected and the samples labeled as one of five sea ice types using knowledge of their spatial context and backscatter intensity:

1. Deformed Multi-Year Ice (MY-D): The deformed features include all ridges, hummocks or surface topography which give a textured appearance to the imagery.

2. Undeformed MY ice (MY-U): Areas of multiyear ice with smooth texture and appearance with no obvious large scale ridging or deformation.

3. Deformed first-Year (FY-D): FY ice in the SIZ with deformed features due to ridging and rafting. This classification allows us to characterize the variability of the FY ice signature, especially of ice in the shear zone.

4. Undeformed FY ice (FY-U): Areas of FY ice in the SIZ with smooth texture and appearance with no obvious deformation features.

5. Lead ice in the PIZ is ice that appears in cracks, fractures and openings in the ice pack. This ice could be in various stages of growth. Our definition of a 'lead' is more of a geometric definition and is a feature which appears as a crack or fracture in the ice. It includes ice (e.g. new, young, grease, frazil, pancake, etc.) with high and low backscatter. This classification allows us to monitor the backscatter variability of ice in the leads.

The sampling method consisted of interactively defining an area on the SAR image with an arbitrary polygon. Wherever possible, large sample populations were chosen to increase the confidence in the estimation of the backscatter statistics. Typically, sample sizes varied from around 30 pixels (0.3 Km^2) in small, narrow leads up to 3000 pixels (30 Km^2) for samples collected over large multiyear floes. Summary statistics (mean and standard deviation) of the backscatter and incidence angle for each sample window were recorded. In this paper, the standard deviation (in dB) is defined as follows:

$$S.D.(dB) = 10log\frac{P_o + P_{S.D.}}{P_o}$$

where P_o and $P_{S.D.}$ are the mean backscattered power and the standard deviation of the backscattered power, respectively. Tables 2 and 3 give the number of samples taken for each ice class in each of the data tracks. The multiyear deformed (MY-D) and lead ice were most heavily sampled. The following sections provide discussions of the backscatter dataset and their temporal and spatial variabilities.

4 Multiyear/Lead Ice Signature

In this section, we discuss the regional, temporal and incidence angle behavior of multiyear and lead ice signatures from the perennial ice zone.

4.1 Multiyear(MY) Ice

The ERS-1 SAR is extremely stable as evidenced by the consistency of multiyear ice backscatter signature presented here. Thus, even though there could be a bias in the observed backscatter cross-section, the sensor and processor calibrations are such that the temporal variation of this bias is slow and small. The histograms of the backscatter of the deformed and undeformed MY samples in Figure 4 show that the two MY ice types differ only in the second moment. Due to the relatively smaller number of undeformed multiyear ice samples and the similarity of the mean backscatter values of the two multiyear ice classes, only the deformed MY ice data is discussed here.

Spatial and Temporal Variability. The spatial and temporal variability of the backscatter signal of the deformed multiyear ice is summarized in Figure 5. The four columns represent the four data tracks while the four rows represent time averages of the backscatter. Orbit adjustment of the ERS-1 satellite was performed during the period DOY 340-365 in 1991 and thus the gap in the data sampling. Figure 6 uses contours to depict the spatial behavior of MY ice backscatter during these same time periods. Several general observations can be made about the data:

1. Backscatter from MY ice increases from the western Beaufort to the Canadian Archipelago.

2. Above 75°N, the backscatter of multiyear ice generally increases with latitude and is especially evident in the western Beaufort. There is a minima at around 75°N (in the western Beaufort) and the backscatter tends to increase toward the southern Beaufort.

3. The minimum and maximum of the sample means are all within 1dB of the population mean.

4. At a given geographic location, the multiyear ice backscatter remains quite stable (within 0.5dB) throughout a given winter.

5. These same trends can be observed in the backscatter data from both winters.

We discuss in more detail each of these observations below. Before we attribute any physical significance to these observations, it is important to consider the limitations of the radar measurements. First, the latitude dependence of the backscatter seems to be a trend observed in the dataset and the change in most cases is approximately 2dB. A sensor/processor effect could account for this observed trend because the ERS-1 SAR goes through almost identical thermal and Doppler histories (i.e. Doppler frequency due to the relative velocity of the phase center of the antenna and its illuminated area on the Earth) along these descending tracks and therefore a systematic gain variation with latitude is probable. To test this hypothesis, the σ_o of multiyear ice from two ascending and two descending pass image sets acquired within a 12 day period at four orbit crossing points were sampled and compared (see Figure 7). The same trend is observed in the ascending pass data and the backscatter values were found to be consistent to within a few tenths of a dB. Since the ERS-1 SAR encounters different thermal and Doppler histories in the ascending tracks, it is unlikely that the observations are sensor/processor induced. (The slightly higher difference between the ascending versus descending backscatter (0.4dB) in the higher

latitudes only enhances the trend and could be due to calibration uncertainties.)

Then, can such persistent features in the data be explained? Assuming we start with an initial latitude dependence in the backscatter data, does ice motion tend to randomize the observed trends? We consider the mean motion of the ice in the Beaufort Sea from October to March. The seasonal mean ice motion in the winter is an expression of the Beaufort Gyre with a magnitude of less than 2cm/sec (east to west motion) near 75°N generally decreasing with latitude [*Colony*, 1990] i.e. northward toward the center of the gyre. With an average ice motion of 2cm/sec, the total ice motion over the period of interest (approximately 160 days) over the Beaufort Sea is approximately 270km, or a few SAR image frames. It is not surprising then that such persistence can be observed in the data.

Along the *ppi* tracks (see Figures 5 and 6) which sample the MY ice near the Canadian Archipelago, the MY ice shows generally higher backscatter values with two backscatter maxima near the location of Prince Patrick Island near 77°N and Banks Island near 73°N. The higher backscatter is probably due to the age and deformation of the ice in this region due to convergence of ice causing extensive pressure ridging of the ice cover. We observed that the SAR images show that the MY floes have a more textured appearance than the floes in the western Beaufort. Comparison of the spatial backscatter contours with mean ice thickness and age contours of the sea ice [*Bourke and McLaren*, 1992; *Colony and Thorndike*, 1985] show correlation of these datasets near the Canadian Archipelago and in the other parts of the Beaufort. The thickness and age near the archipelago is twice the basinwide mean age and thickness. This provides evidence that the deformation in the MY ice due to the mechanical processes in this region is responsible for the observed backscatter contrast between MY ice in this region and the other parts of the Beaufort. We also observe (Figures 6b and 6c) the westward advection of the higher backscatter contours most probably due

the transport of the thicker, more deformed or higher backscatter MY sea ice from the Canadian Archipelago to the western Beaufort.

Cavalieri et al.[1991] observed that the anomalously low multiyear ice concentration predicted by SSM/I compared with KRMS data near the coastal regions of the Canadian Archipelago may be due to the significant amount of saline first-year ice being piled up onto multiyear floes. The repeated lead formation and collapse due to the intense deformation in this region was suggested as a mechanism which could increase the mean salinity of the surface layer due to the entrapment of first-year ice on the surface of multiyear floes, thus explaining the bias of the passive microwave signature toward first year ice. From an active microwave signature stand point, the effect of a rougher higher salinity surface could certainly increase the mean backscatter, although we expect that such an effect to only be obvious at the edges of floes and it is not clear how extensive such an effect is away from the edges of the large floes.

We offer speculations as to the physical significance of the latitude dependence observed in the western Beaufort. The MY backscatter in this region is generally lower than that observed near the Canadian Archipelago, with the general backscatter increasing with latitude. From a microscopic ice characteristics point of view, the salinity, air bubbles and temperature are the most important factors which affect the backscatter of multiyear ice. Multiyear ice has a fairly narrow range of salinity and is typically less than 2ppt [*Gow et al.*, 1987]. With salinity alone, it takes a rather large change in salinity of 3ppt to explain a 1.5dB difference in the backscatter [*Nghiem*, 1992 *Personal Communication*]. Thus, it seems difficult to attribute the observation to a salinity effect. Variations in the size of air bubbles could certainly affect the backscatter but we do not have any current evidence that size distribution is dependent on geographic location. Backscatter variation due to thermal modulation is probably small under the *winter* conditions considered here. On a larger scale,

over the areal extent of the sample windows used to calculate the mean backscatter, the measurement represents backscatter contributions from frozen melt ponds, undeformed and deformed (e.g. ridges, hummocks, etc.) ice features all which are not resolved at the resolution of the data product used. A higher fractional area in frozen meltponds tends to decrease the overall backscatter whereas higher fractional areas of deformed features tends to enhance backscatter. If the basinwide mean thickness of the ice away from the islands are approximately the same [*Bourke and McLaren*, 1992], then the degree of meltponding on multiyear floes can more likely explain the backscatter differences of the magnitude observed here. Ponding on old ice occupies between 25-45% of the surface [*Carsey*, 1985]. If the σ_o of multiyear ice were -10dB and that of multiyear ice with superimposed frozen meltpond were -20dB [*Onstott*, 1992], a 20% decrease in areal coverage of refrozen meltponds can account for the higher backscatter observed at higher latitudes. There is little observational literature on fractional frozen meltpond coverage of multiyear ice in the winter Arctic. It seems more likely that the effect is a combination of fractional melt pond coverage and deformation, although there are insufficient field observations to resolve this hypothesis at this time.

In both years, there is a minimum at around 75°N in the western Beaufort below which the backscatter trends higher. These higher values may reflect increased ice deformation frequently observed in this region owing to the shear zone brought about by converging and diverging ocean currents [*Weeks et al.*, 1980]. We note here that this minima roughly coincides with the general limit of the summer ice extent. As mentioned above, this observation may also result from the advection of the higher backscatter MY sea ice from the eastern Beaufort. This effect is unexplained at this time.

The temporal behavior of MY backscatter from the winter of 1991/92 is shown in Figure 8. These plots show the mean backscatter values from multiyear ice samples for all images within each orbit in the four tracks (sampled every 12 days). The plots show a fairly consistent signal with some variability in the earlier orbits. However, the data samples were taken at different latitudes in each orbit, thereby suggesting that the averages may be weighted by the latitudinal backscatter dependence. By taking the average latitude of the sampled pixels in each orbit, an estimate of this variation can be made for each orbit from 1^o binned values. After taking this variation into account, the normalized mean backscatter values are shown in Figure 8b. Note the greater consistency of the signal in the earlier orbits. The overall signal has only slight variations and shows the multiyear ice to be a temporally stable backscatter target (with spatial variations) throughout this time period.

Comparsion with Scatterometer Data. The multiyear ice backscatter observed here is approximately 1.5dB lower than the C-band scatterometer measurements in *Onstott* [1992]. Athough this is within the absolute calibration uncertainty of the ERS-1 data products, this could be due to the resolution disparity between the ERS-1 SAR resolution element and the scatterometer footprint as mentioned earlier. Again, it is expected that SAR image backscatter observations are modulated to a higher degree by mixtures of ice types compared with scatterometer samples and that observations at the larger scale could be biased or have larger variance in backscatter than the pure ice type. The incidence angle dependence of the backscatter (dB/degree of incidence angle) are derived from linear regressions of all the sample means. As expected, there is a weak dependence on incidence angle over the range of incidence angles observed by ERS-1. The slopes range from -0.03 to -0.1 dB/deg (see Figure 9) and are comparable to scatterometer observations.

4.2 Lead Ice

The histograms of the lead ice backscatter samples are shown in Figure 10. The lead ice samples give a mean of approximately -17 to -18dB. The spatial and temporal variability of lead ice in the PIZ are shown in Figures 11 and 12. The arrangement of the plots is identical to those in Figures 5 and 8. A larger range of backscatter, approximately 3dB, is seen compared to that observed for multiyear ice.

The amount of variability can be attributed to the range of ice types that can exist in leads. The lead ice category covers a wide range of ice, with ages ranging from a few hours to possibly months. This large range of ice thicknesses and ages would promote a higher scatter in the values. It is also important to note that some of the lead ice signatures are close to the noise floor of the system. Because of this variability in the backscatter of lead ice (ice growth is continually altering the signatures), we did not explore and indeed did not observe any spatial and temporal trend in this ice type which contains a mixture of different types of ice. The temporal signatures (Figure 12), however, show that the mean observed here is fairly stable throughout the season and that there is a fairly high contrast between the MY and lead ice.

5 First-Year Ice Signature

The remaining two ice types (deformed first-year (FY-D), undeformed first-year (FY-U)) are discussed in this section. Under cold winter conditions where the ice surface and snow cover are dry, these two FY ice types are visually discernable. The undeformed FY-U type has no major deformation features while the FY-D type contains extensively ridged ice. The visual sampling of the backscatter statistics is based on these criteria. As discussed, the spatial sampling of deformed and undeformed first-

year ice types is mostly restricted to the seasonal ice zones (below 75°) and thus have a significantly smaller number of samples (Table 2). Also, we would like to note here that the separation of these two ice types is more ambiguous due to the seasonal nature of this ice. These ice types are not as stable and their signatures tend to develop based on their thickness and age. Due to this variability, there is much less we can say about their spatial behavior and even less of the temporal behavior due to our current inability to observe the signature evolution of the same FY ice floe for an extended period of time. The backscatter histograms for these two FY ice types are shown in Figure 13.

Deformed First-year Ice. This deformed ice is usually associated with ridged and rafted ice where the backscatter is dominated by manifestations of this deformation. The mean backscatter of this ice type is approximately -14dB and covers the range of σ_o between MY ice and undeformed FY or lead ice (see Figure 13). The mean standard deviation of the samples is 1.2dB. As expected, there is almost no dependence of the backscatter on incidence angle as a result of the deformed ice surface (see Figure 9). These observations are consistent with that of the scatterometer measurements of *Onstott* [1992].

Undeformed First-year Ice. The undeformed first-year ice (FY-U) is also limited to lower latitudes. The mean backscatter of this ice type is approximately -17 to -18 dB which is similar to the mean of the lead ice in the PIZ. The mean standard deviation of the samples is 1.6dB. Figure 9 shows that the dependence of the backscatter on incidence angle is higher (0.15dB/deg - 0.37dB/deg) than FY-D ice and MY ice, probably due to the surface scatter contribution of a relatively undeformed and saline ice surface.

6 Summary

We have summarized the C-band VV backscatter signatures of sea ice in the Beaufort Sea during the winter of 1991 and the early winter of 1992. The observations have shown that MY ice signatures although temporally stable vary with the region studied in this paper. The subtle spatial structure of MY ice backscatter signature in the Beaufort can be observed because of the stability of the ERS-1 SAR sensor and the SAR image formation system at the Alaska SAR Facility. The spatial structure of MY ice backscatter in the Beaufort can be correlated to physical processes, some of which are suggested in this paper. For example, the higher backscatter of MY ice near the Canadian Archipelago is an effect most likely due to extensive pressure ridging due in turn to ice convergence at the land boundaries. We have speculated on the cause of spatial structure in other regions although there do not exist observations to test these hypotheses. Based on MY ice signature observations from two winters, this spatial structure remains substantially unchanged for this region. We have also characterized the range of backscatter of FY ice by sampling deformed and undeformed FY ice. Except for highly deformed FY ice, the FY ice signature also remain quite stable through the winter. Therefore, the claim of consistent contrast betweem MY and FY ice during the winter season is borne out by the results shown here. Under these winter conditions, the identification of principal ice types (MY and FY) can be done with relative ease. The lower backscatter ice in some of the frozen leads is indicative of thinner ice types although observation of these ice types is limited by the type of radar data (single frequency and polarization) and the method of data collection used here. Without in-situ and other sensor observations, it remains a difficult task to unambiguously identify ice types other than the ones studied in this paper. We have also limited our observations to a very small region of the Arctic in this paper. We intend to direct our attention to other areas (e.g. Chukchi sea and E. Siberian

sea, etc.) in our future work.

Acknowledgments

The authors wish to thank F. Carsey, B. Holt, M. Drinkwater and S. Nghiem of JPL for their valuable comments on the manuscript and R. LeeJoice for compiling the dataset for this study. This work was carried out at the Jet Propulsion Laboratory, California Institute of Technology under contract with the National Aeronautics and Space Administration.

7 References

Bourke, R. and A. S. McLaren, Contour Mapping of Arctic Basin Ice Draft and Roughness Parameters, *J. Geophys. Res.*, 92(C11), 17715-17728, 1992.

Carsey, F. D., Summer Arctic sea ice character from satellite microwave data, *J. Geophys. Res.*, 90(C3), 5015-5034, 1985.

Carsey, F, Review and status of remote sensing of sea ice, *IEEE J. Oceanic Eng.*, 14(2), 127-138, 1989.

Cavalieri, D. J., B. A. Burns, and R. G. Onstott, Investigation of the effects of summer melt on the calculation of sea ice concentration using active and passive microwave data, *J. Geophys. Res.*, 95(C4), 5339-5369, 1990.

Cavalieri, D. J., J. P. Crawford, M. R. Drinkwater, D. T. Eppler, L. D. Farmer, R. R. Jentz, and C. C. Wackerman. Aircraft Active and Passive Microwave Validation of Sea Ice Concentration from the Defence Meteorological Satellite Program Special Sensor Microwave Imager. *J. Geophys. Res*, 96(C12), 21989-22008, 1991.

Colony, R. and A. Thorndike, Sea ice motion as a drunkard's walk, *J. Geophys. Res.*, 90(C1), 965-974, 1985.

Colony, R., Seasonal mean ice motion in the Arctic Basin, *Proc. of International Conference on the Role of the Polar Regions in Global Change*, Fairbanks, AK. 290-300, 1990.

Drinkwater, M. R., LIMEX '87 ice surface characteristics: Implications for C-band SAR backscatter signatures, *IEEE Trans. Geosci. Remote Sensing*, Vol. 47, pp 501-513, Sept. 1989.

Drinkwater, M., R. Kwok, D. Winebrenner, and E. Rignot, Multi-frequency Polarimetric SAR Observations of Sea Ice, *J. Geophys. Res.*, 96 (C11), 20,679-20,698, 1991.

Fatland, R. and A. Freeman, Calibration and Change Detection of ASF/ERS-1 Image Data, *Proc. IGARSS 1992.*

Gray, A. L., R. K. Hawkins, C. E. Livingston, L. D. Arsenault and W. M. Johnstone, Simultaneous Scatterometer and Radiometer Measurements of Sea-Ice Microwave Signatures, *IEEE J. of Oceanic Engr.*, OE-7(1), 20-32, 1982.

Gow, A., S. A. Arcone, S. G. McCrew, Microwave and Structural Properties of Saline Ice, *CRREL* Report 87-20, 1987.

Holt, B. and S. A. Digby, Processes and imagery of first-year fast sea ice during the melt season, *J. Geophys. Res.*, 90(C3), 5045-5062, 1985.

Kim, Y. S., R. K. Moore, R. G. Onstott, and S. Gogineni, Towards the identification of optimum radar parameters for sea-ice monitoring, *J. Glaciol.*, 31(109), 214-219, 1985.

Kwok, R., E. Rignot, B. Holt and R. G. Onstott, Identification of Sea Ice Type in Spaceborne SAR Data, *J. Geophys. Res.*, 97 (C2), 2391-2402, 1992.

Livingstone, C. E., R. G. Onstott, L. D. Arsenault, A. L. Gray, and K. P. Singh, Microwave sea-ice signatures near the onset of melt, *IEEE Trans. Geosci. Remote Sens.*, GE-25(2), 174-187, 1987a.

Livingstone, C. E., K. P. Singh, and A. L. Gray, Seasonal and regional variations of active/passive microwave signatures of sea ice, *IEEE Trans. Geosci. Remote Sens.*, GE-25(2), 159-173, 1987b.

Livingstone, C. E., and M. R. Drinkwater, Spring time C-band SAR backscatter signatures of Labrador Sea marginal ice: Measurements vs. modelling predictions, *IEEE Trans. Geosci. Remote Sens.*, GE-29(1), 29-41, 1991.

Lyden, J. D., B. Burns and A. L. Maffet, Characterization of Sea Ice Types Using Synthetic Aperture Radar, *IEEE Trans. Geosci. Electron.*, GE-22(5), 431-439, 1984.

Onstott, R. G., SAR and Scatterometry Signatures of Sea Ice, in *Microwave Remote Sensing of Sea Ice* edited by Frank D. Carsey, 73-104, AGU Geophysical Monograph 68, Washington, D. C.

Onstott, R. G., T. C. Grenfell, C. Matzler, C. A. Luther and E. A. Svendsen, Evolution of the Microwave Sea ice Signatures During Early Summer and Midsummer in the Marginal Ice Zone, *J. Geophys. Res.*, *92*(C7) 6825-6835, 1987.

Onstott, R. G. and S. P. Gogineni, Active Microwave Measurements of Arctic Sea Ice Under Summer Conditions, *J. Geophys. Res.*, *90*(C3) 5035-5044, 1985.

Onstott, R. and R. A. Shuchman, Radar Backscatter of Sea Ice During Winter, *Proceedings of IGARSS '88 Symposium*, Edinburgh, Scotland, 13-16 Sept., Vol. 2, 1115-1118, 1988.

Onstott, R. G., R. K. Moore, S. Gogineni and C. V. Delker, Four Years of Low Altitude Sea Ice Broadband Backscatter Measurements, *IEEE J. Oceanic Eng.*, OE-7(1), 44-50, 1982.

Onstott, R. G., R. K. Moore and W. F. Weeks, Surface-based Scatterometer Results of Arctic Sea ice, *IEEE Trans. Geosci. Electron.*, GE-17(3), 78-85, 1979.

Shokr, M., Evaluation of Second-Order Texture Parameters for Sea Ice Classification From Radar Images, *J. Geophys. Res.*, 96 (C6), 10,625-10,640, 1991.

Ulaby, F., R. K. Moore and A. K. Fung, *Microwave Remote Sensing: Active and Passive*, Vol. III, Artech House, Inc., 1986.

Wackerman, C. C., R. R. Jentz and R. A. Shuchman, Sea Ice Type Classification of SAR Imagery, *Proceedings of IGARSS '88 Symposium*, Edinburgh, Scotland, 13-16 Sept., Vol. 2, 425-428, 1988.

Weeks, W. F., W. B. Tucker III, M. Frank and S. Fungcharoen, Characterization of the surface roughness and floe geometry of sea ice over the continental shelves of the Beaufort and Chukchi seas in *Sea Ice Processes and Models*, edited by R. S. Pritchard, pp. 283-299, University of Washington Press, Seattle, 1980.

Winebrenner, D. P., L. Tsang, B. Wen, and R. West, Sea-ice characterizationmeasurements needed for testing of microwave remote sensing models, *IEEE J. Oceanic. Eng.*, 14(2), 149-157, 1989.

ptb		prb		alc		ppi	
DOY	no. of images	DOY	no. of images	DOY	no. of images	DOY	no. of images
---	---	299	11	297	19	---	---
310	3	311	15	309	12	---	---
322	14	323	2	321	3	---	---
334	15	335	15	339	16	---	---
5	12	6	17	4	11	---	---
17	18	18	18	16	20	17	17
29	17	---	---	---	---	29	17
41	17	42	17	---	---	---	---
53	17	---	---	52	19	53	17
65	19	66	20	---	---	---	---
77	19	78	20	76	19	---	---
89	19	90	20	88	18	89	17
312	12	313	16	314	14	315	8
359	18	360	17	364	18	359	10
200 images		188 images		169 images		86 images	
Total = 643 images							

Table 1. Times and numbers of sampled images

	ptb	prb	alc	ppi	all
MY_D	2677	2480	2317	1141	8615
MY_U	205	371	300	273	1149
FY_D	152	57	26	0	235
FY_U	126	113	96	84	419
Lead	885	858	804	423	2969

Table 2. Number of samples for each ice type (Winter '91)

	ptb	prb	alc	ppi	all
MY_D	411	482	449	180	1522

Table 3. Number of samples for each ice type (Winter '92)

Figure Captions

Figure 1. Coverage of the four descending ERS-1 tracks (within the ASF mask) during the Ice phase.

Figure 2. Region-wide 1000mb air temperature record (°C). For convenience, the abscissa is plotted as 1992 day-of-year (DOY), using negative values during 1991. (a) Region wide temperature record. (b) Averaged temperature distribution 1991:DOY 320-365. (c) Averaged temperature distribution 1992:DOY 1-45. (d) Averaged temperature distribution 1992:DOY 46-91. (e) Averaged temperature distribution 1992:DOY 321-366.

Figure 3. ERS-1 SAR image showing sea ice in the Beaufort Sea (Copyright ESA 1992).

Figure 4. Histograms of mean and standard deviation of Deformed MY (MY-D) and Undeformed MY (MY-U) ice backscatter. (a) Mean backscatter of MY-D. (b) Standard deviation of backscatter of MY-D data samples. (c) Mean backscatter of MY-U. (d) Standard deviation backscatter of MY-U data samples. Binning intervals are 0.4 dB and 0.1 dB for the mean and standard deviation plots, respectively. (n = number of points in dataset; mean = mean backscatter in dB; stdev = standard deviation in dB)

Figure 5. Spatial and temporal behavior of multiyear sea ice. The solid bold line in each plot shows the mean backscatter of all pixels within a 1° latitude bin plotted at their average latitude. The dotted lines show the minimum and maximum sample means found within that latitude bin. (a) ptb 1991 DOY 315-340; (b) prb 1991 DOY 315-340; (c) alc 1991 DOY 315-340; (d) ppi 1991 DOY 315-340; (e) ptb 1992 DOY 5-45; (f) prb 1992 DOY 5-45; (g) alc 1992

DOY 5-45; (h) ppi 1992 DOY 5-45; (i) ptb 1992 DOY 45-90; (j) prb 1992 DOY 45-90; (k) alc 1992 DOY 45-90; (l) ppi 1992 DOY 45-90; (m) ptb 1992 DOY 315-365; (n) prb 1992 DOY 315-365; (o) alc 1992 DOY 315-365; (p) ppi 1992 DOY 315-365.

Figure 6. Spatial contours of mean and standard deviation of MY backscatter data from winter of 1991/92 (1991 DOY 315 through 1992 DOY 90) and winter of 1992 (1992 DOY 315-365). (a) 1991 DOY 315-340. (b) 1992 DOY 5-45. (c) 1992 DOY 45-90. (d) Winter of 1991/92. (e) Winter of 1992 (1992 DOY 315-365).

Figure 7. Comparison of MY samples take from overlapping ascending and descending passes at four different latitudes. The mean difference is shown with each figure. (Each point represents a distinct floe sampled in both images.)

Figure 8. Temporal behavior of Multiyear ice backscatter from the winter of 1991. (a) Plot of MY σ_o vs t. (b) Plot of MY σ_o vs t (after normalization of latitude backscatter dependence).

Figure 9. Incidence angle behavior of deformed MY ice backscatter. The slope and number of points used in the regression are shown with each plot.

Figure 10. Histograms of mean and standard deviation of Lead ice backscatter. (a) Histogram of mean backscatter of Lead ice. (b) Histogram of standard deviation backscatter of Lead ice data samples. Binning intervals are 0.4 dB and 0.1 dB for the mean and standard deviation plots, respectively. (n = number of points in dataset; mean = mean backscatter in dB; stdev = standard deviation in dB)

Figure 11. Spatial and temporal behavor of Lead ice. The solid bold line in each plot shows the mean backscatter of all pixels within a 1^o latitude bin plotted at their average latitude. The dotted lines show the minimum and maximum sample means found within that latitude bin. (a) ptb 1991 DOY 315-340; (b)

prb 1991 DOY 315-340; (c) alc 1991 DOY 315-340; (d) ppi 1991 DOY 315-340; (e) ptb 1992 DOY 5-45; (f) prb 1992 DOY 5-45; (g) alc 1992 DOY 5-45; (h) ppi 1992 DOY 5-45; (i) ptb 1992 DOY 45-90; (j) prb 1992 DOY 45-90; (k) alc 1992 DOY 45-90; (l) ppi 1992 DOY 45-90.

Figure 12. Temporal behavior of Lead ice backscatter from the winter of 1991.

Figure 13. Histograms of mean and standard deviation of FY ice backscatter. (a) Mean backscatter of FY-D. (b) Standard deviation of backscatter of FY-D data samples. (c) Mean backscatter of FY-U. (d) Standard deviation of backscatter of FY-U data samples. Binning intervals are 0.4 dB and 0.1 dB for the mean and standard deviation plots, respectively. (n = number of points in dataset; mean = mean backscatter in dB; stdev = standard deviation in dB)

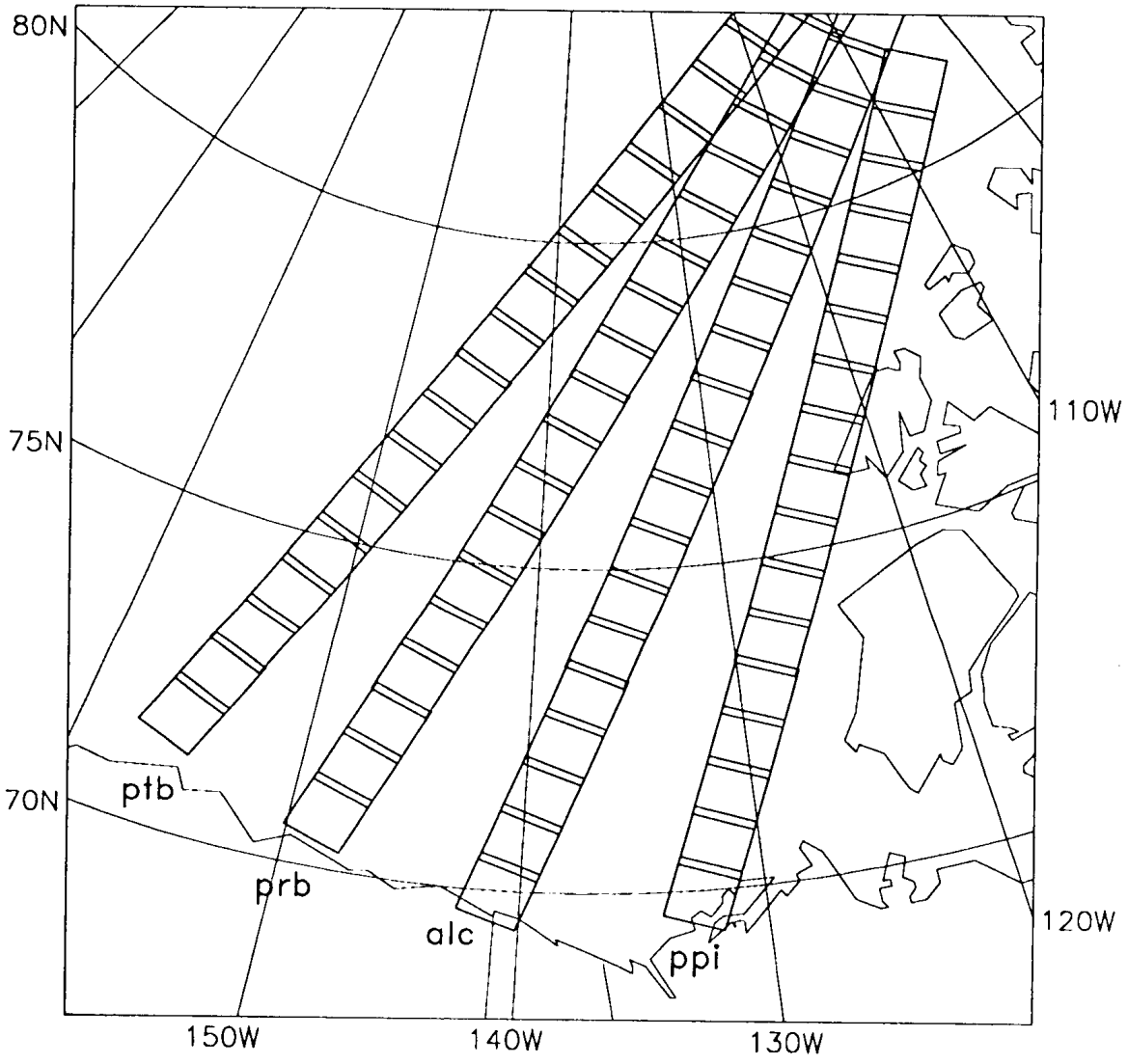
80N
75N
70N
110W
120W
150W
140W
130W
ptb
prb
alc
ppi

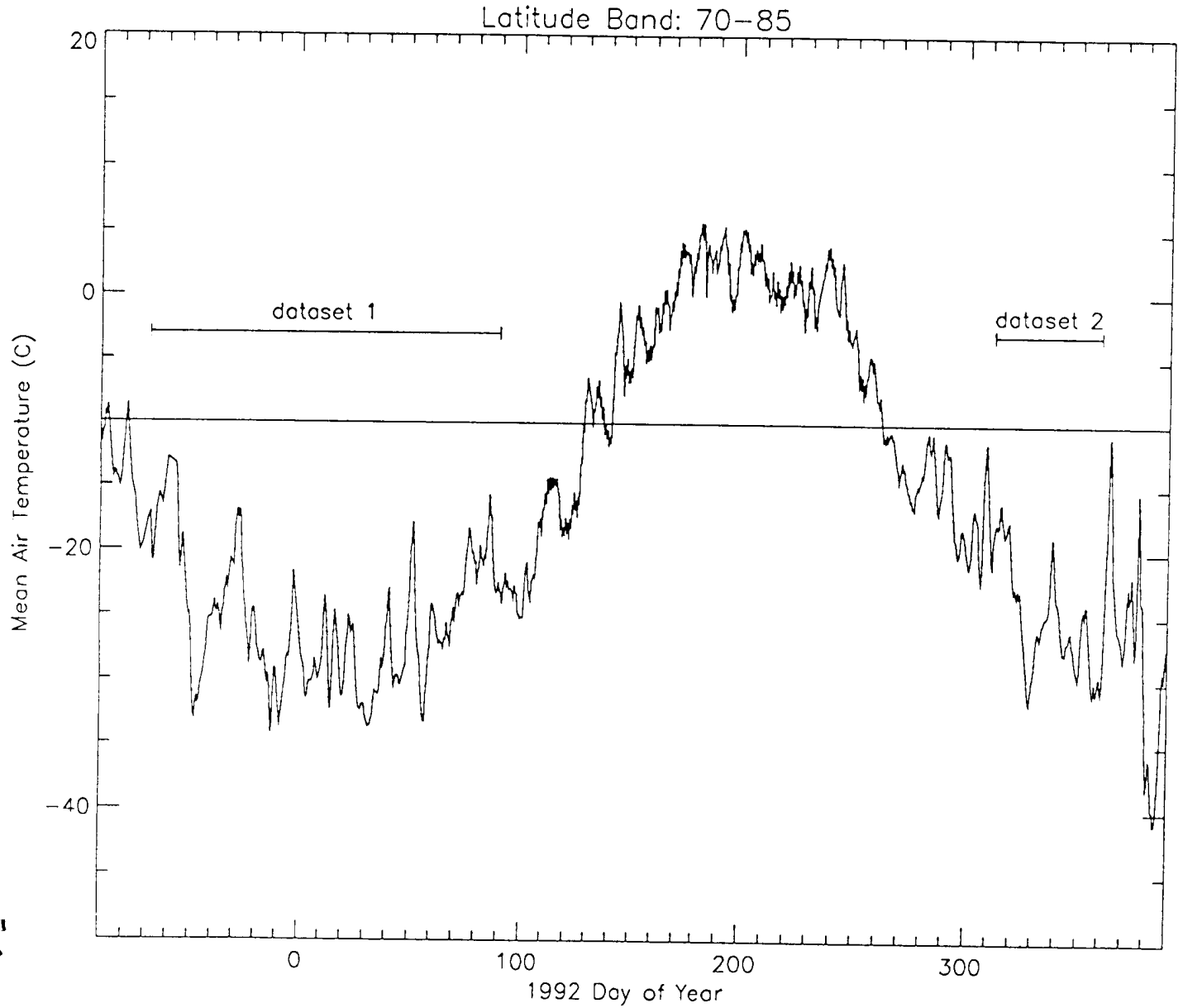
Latitude Band: 70–85
20
0
−20
−40
dataset 1
dataset 2
Mean Air Temperature (C)
0
100
200
300
1992 Day of Year

F.2

1991: DOY 320–365

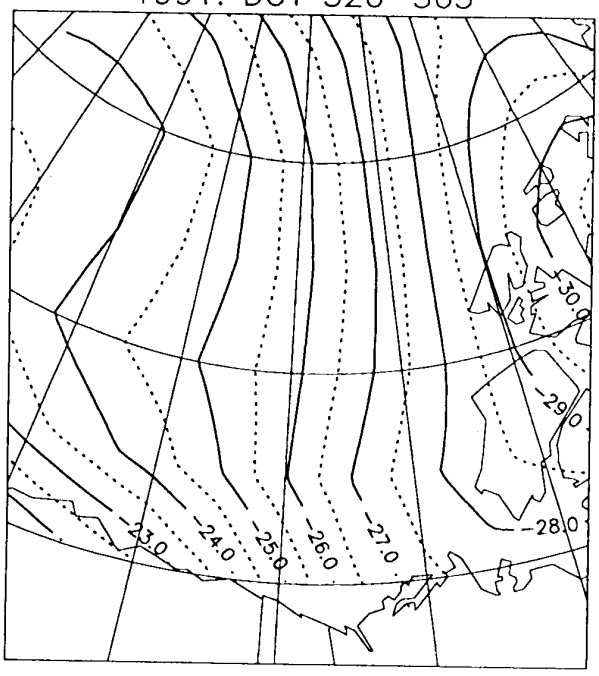

1992: DOY 1–45

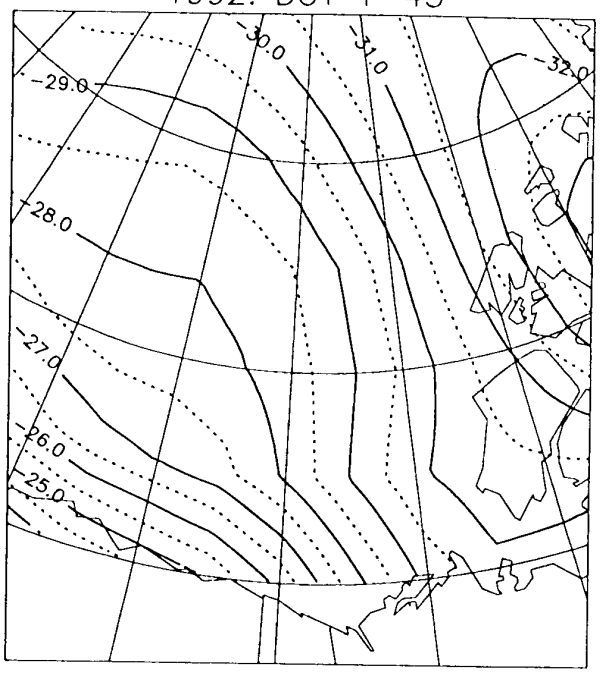

1992: DOY 46–91

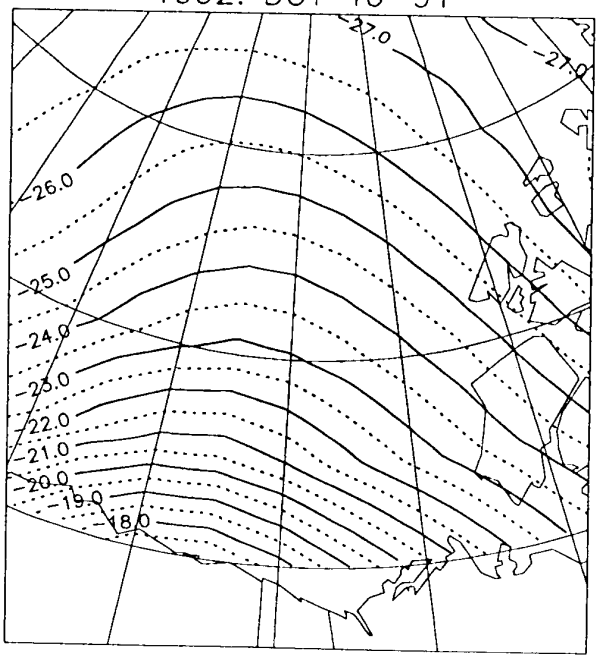

1992: DOY 321–366

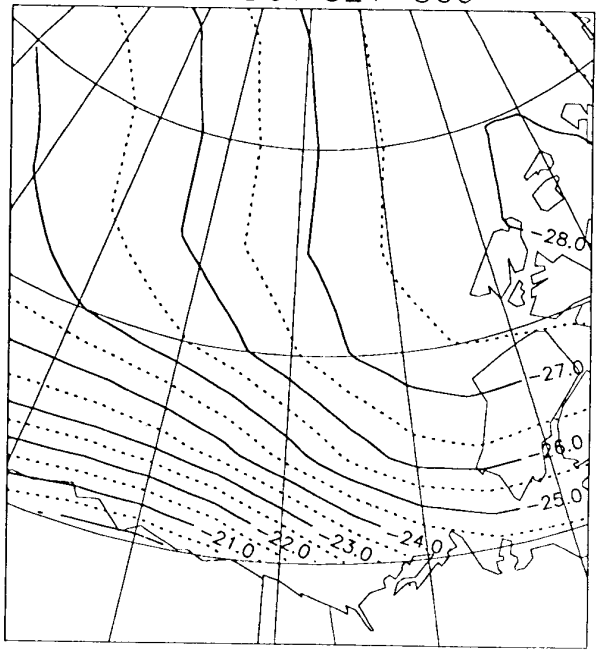

F. 2

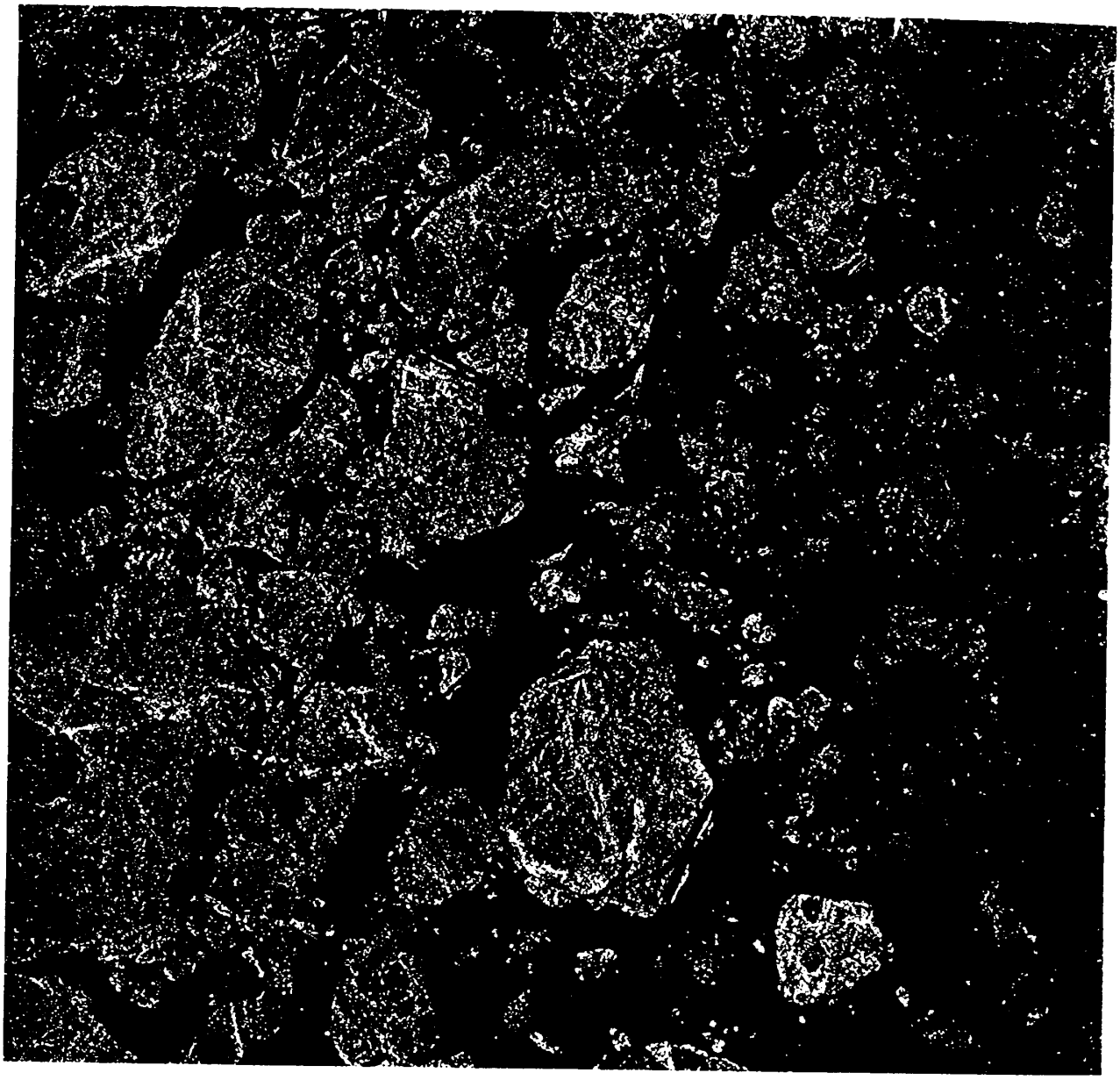

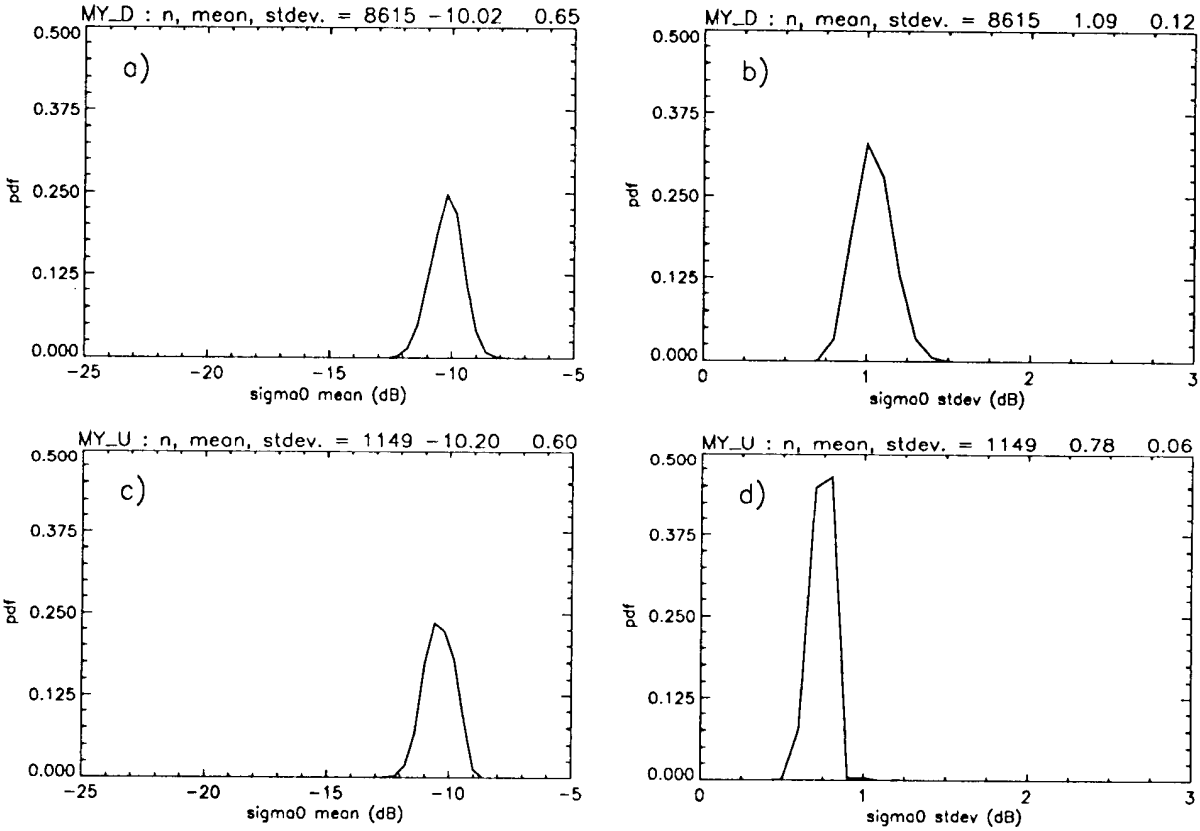
MY_D : n, mean, stdev. = 8615 -10.02 0.65
a)
pdf
sigma0 mean (dB)
MY_D : n, mean, stdev. = 8615 1.09 0.12
b)
pdf
sigma0 stdev (dB)
MY_U : n, mean, stdev. = 1149 -10.20 0.60
c)
pdf
sigma0 mean (dB)
MY_U : n, mean, stdev. = 1149 0.78 0.06
d)
pdf
sigma0 stdev (dB)

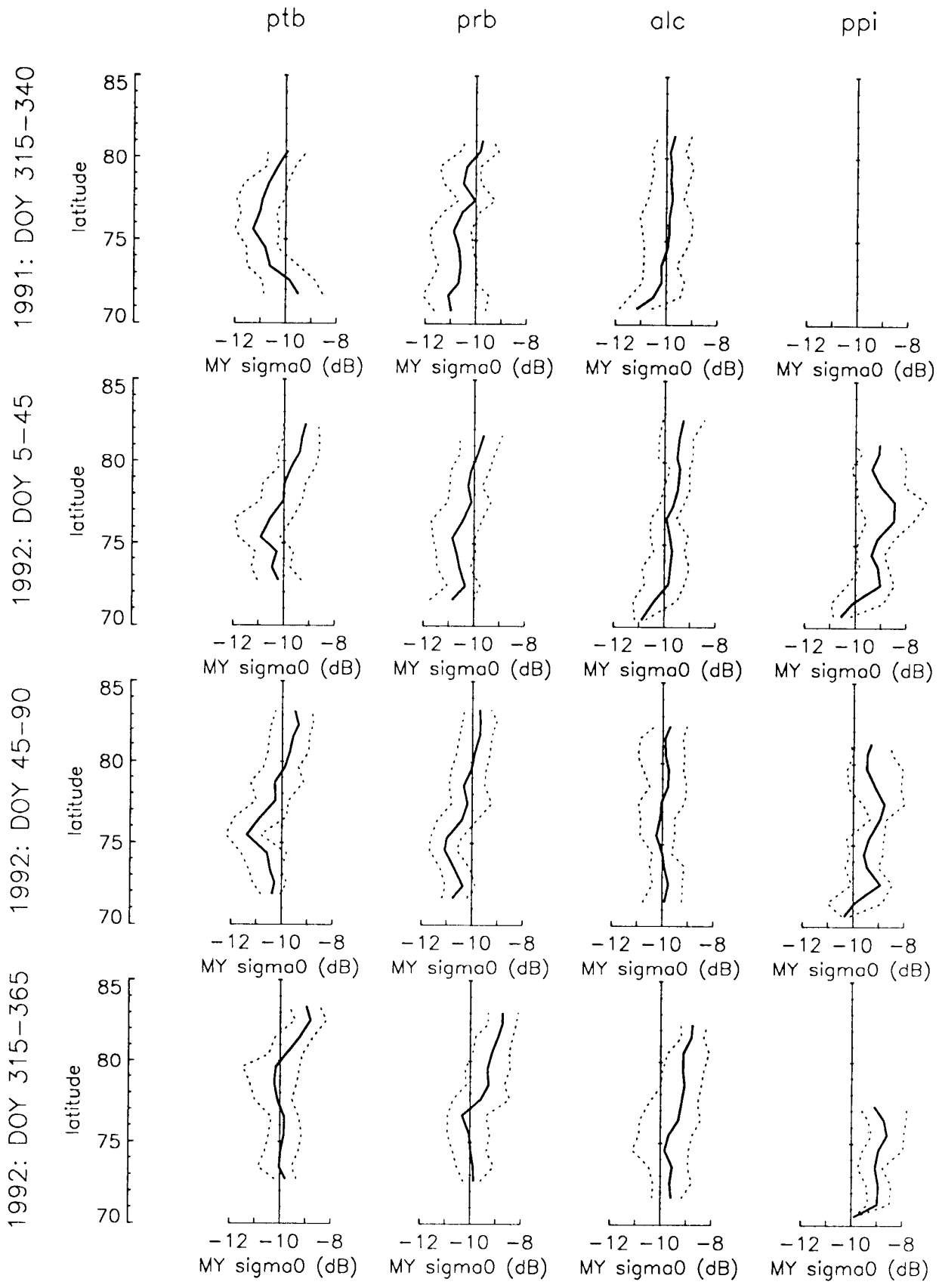
ptb
prb
alc
ppi
1991: DOY 315–340
1992: DOY 5–45
1992: DOY 45–90
1992: DOY 315–365
latitude
85
80
75
70
−12 −10 −8
MY sigma0 (dB)

a)

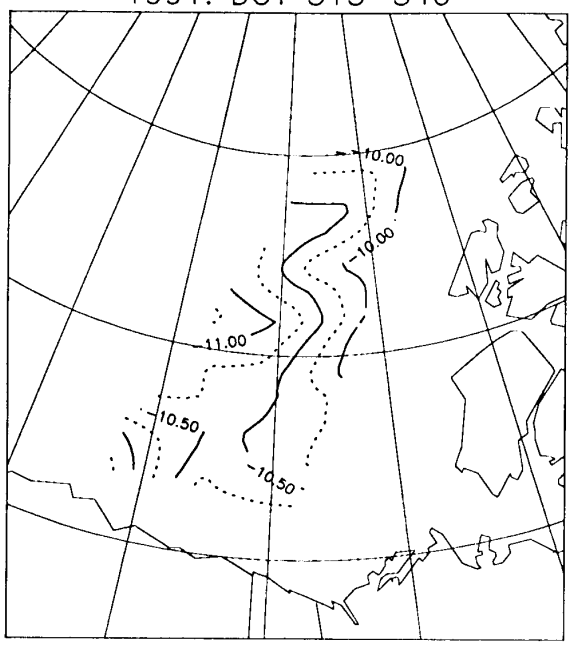

mean

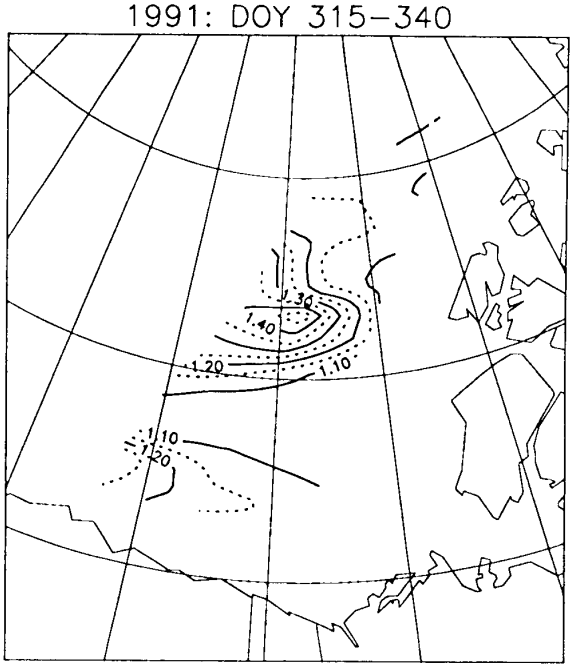

standard deviation

b)

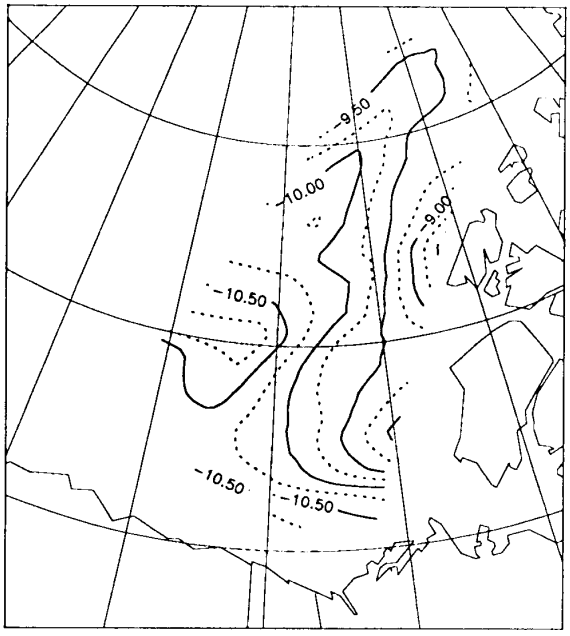

mean

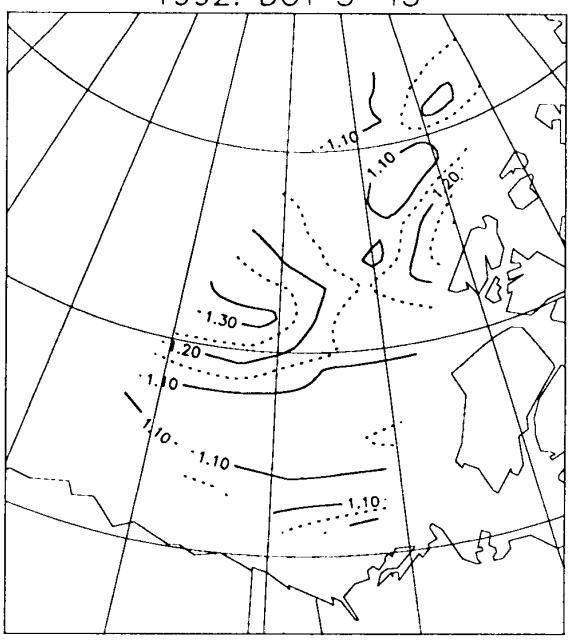

standard deviation

c)

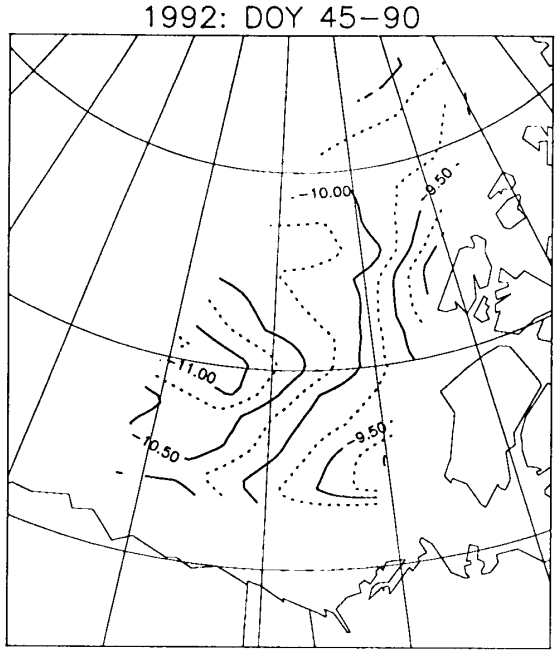

mean

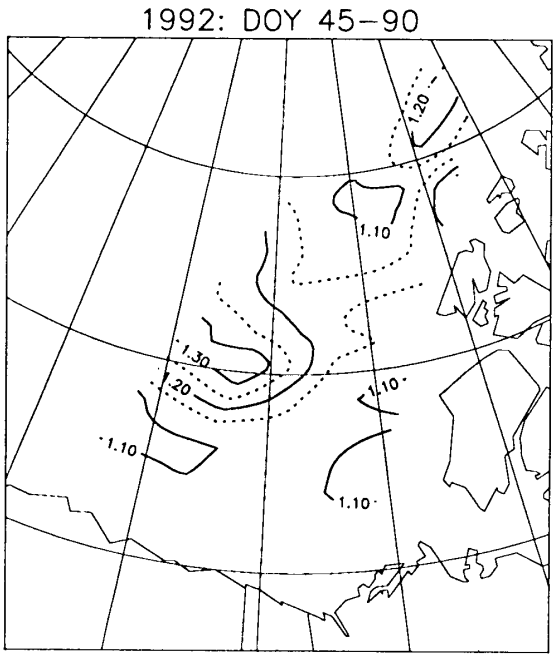

standard deviation

d)

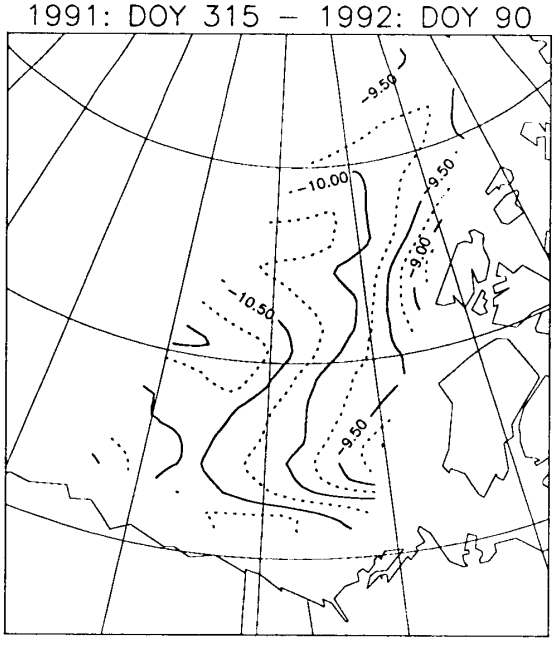

mean

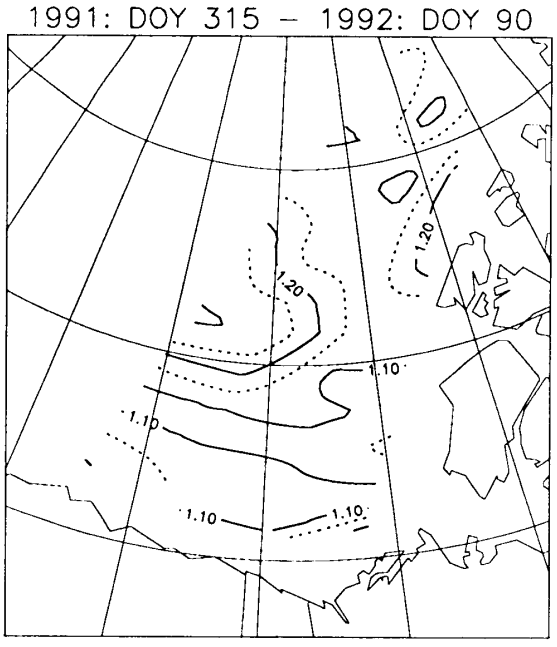

standard deviation

e)

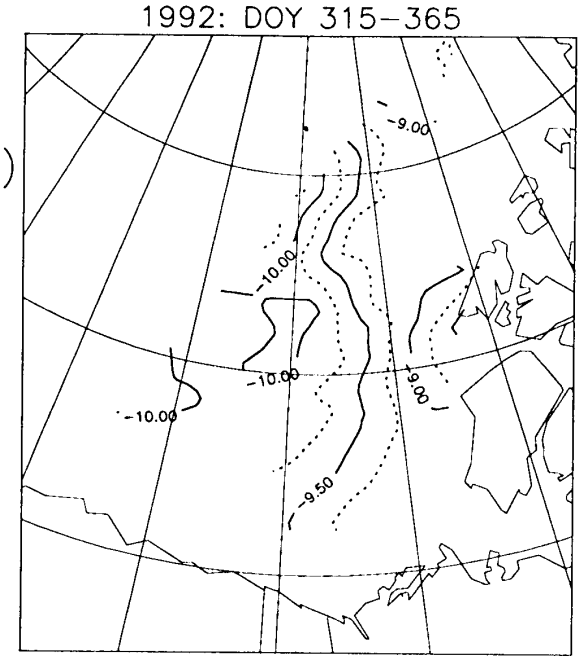

mean

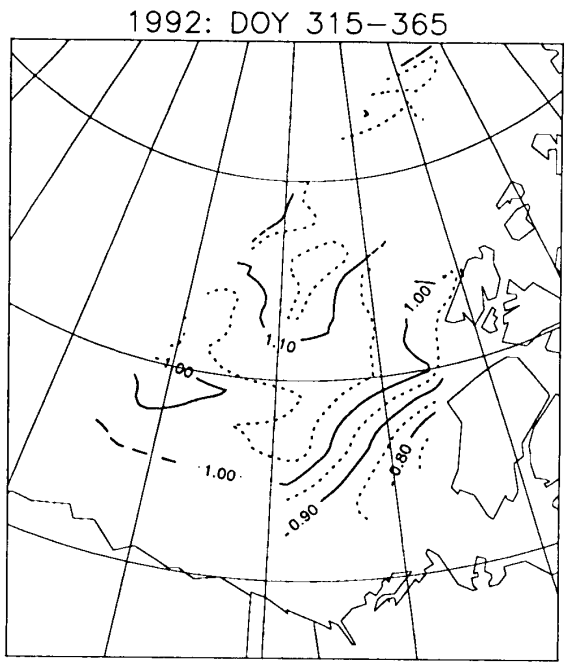

standard deviation

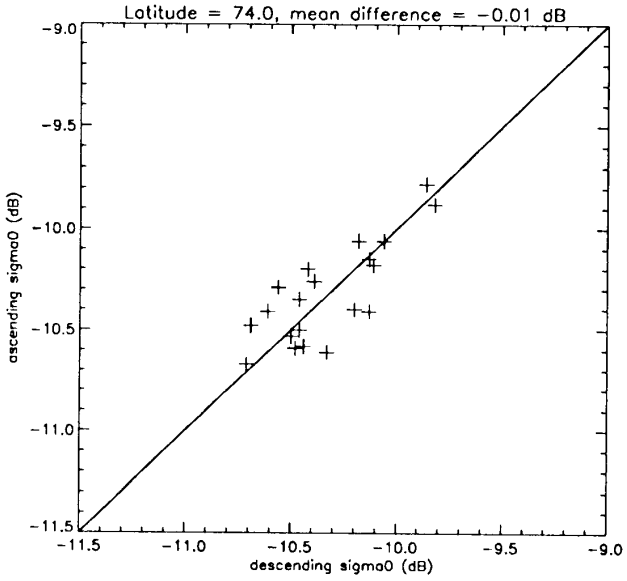
Latitude = 74.0, mean difference = −0.01 dB
ascending sigma0 (dB)
descending sigma0 (dB)
−9.0
−9.5
−10.0
−10.5
−11.0
−11.5

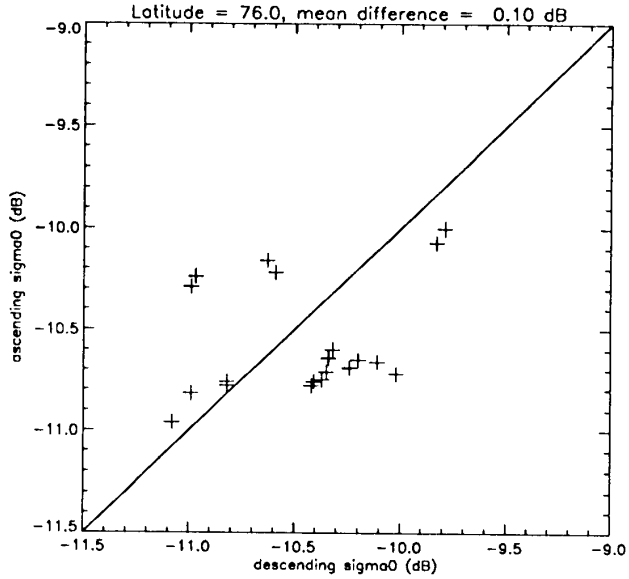
Latitude = 76.0, mean difference = 0.10 dB
ascending sigma0 (dB)
descending sigma0 (dB)
−9.0
−9.5
−10.0
−10.5
−11.0
−11.5

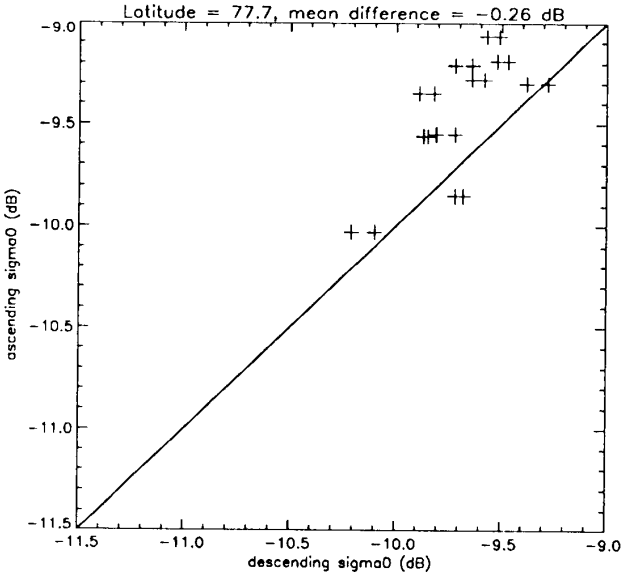
Latitude = 77.7, mean difference = −0.26 dB
ascending sigma0 (dB)
descending sigma0 (dB)
−9.0
−9.5
−10.0
−10.5
−11.0
−11.5

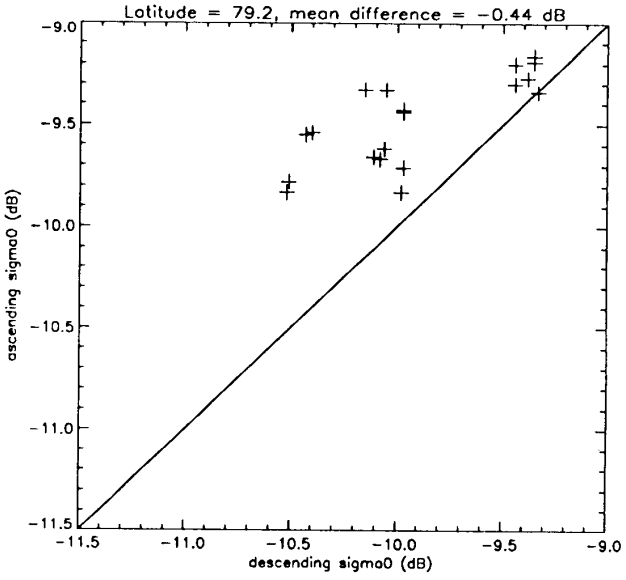
Latitude = 79.2, mean difference = −0.44 dB
ascending sigma0 (dB)
descending sigma0 (dB)
−9.0
−9.5
−10.0
−10.5
−11.0
−11.5

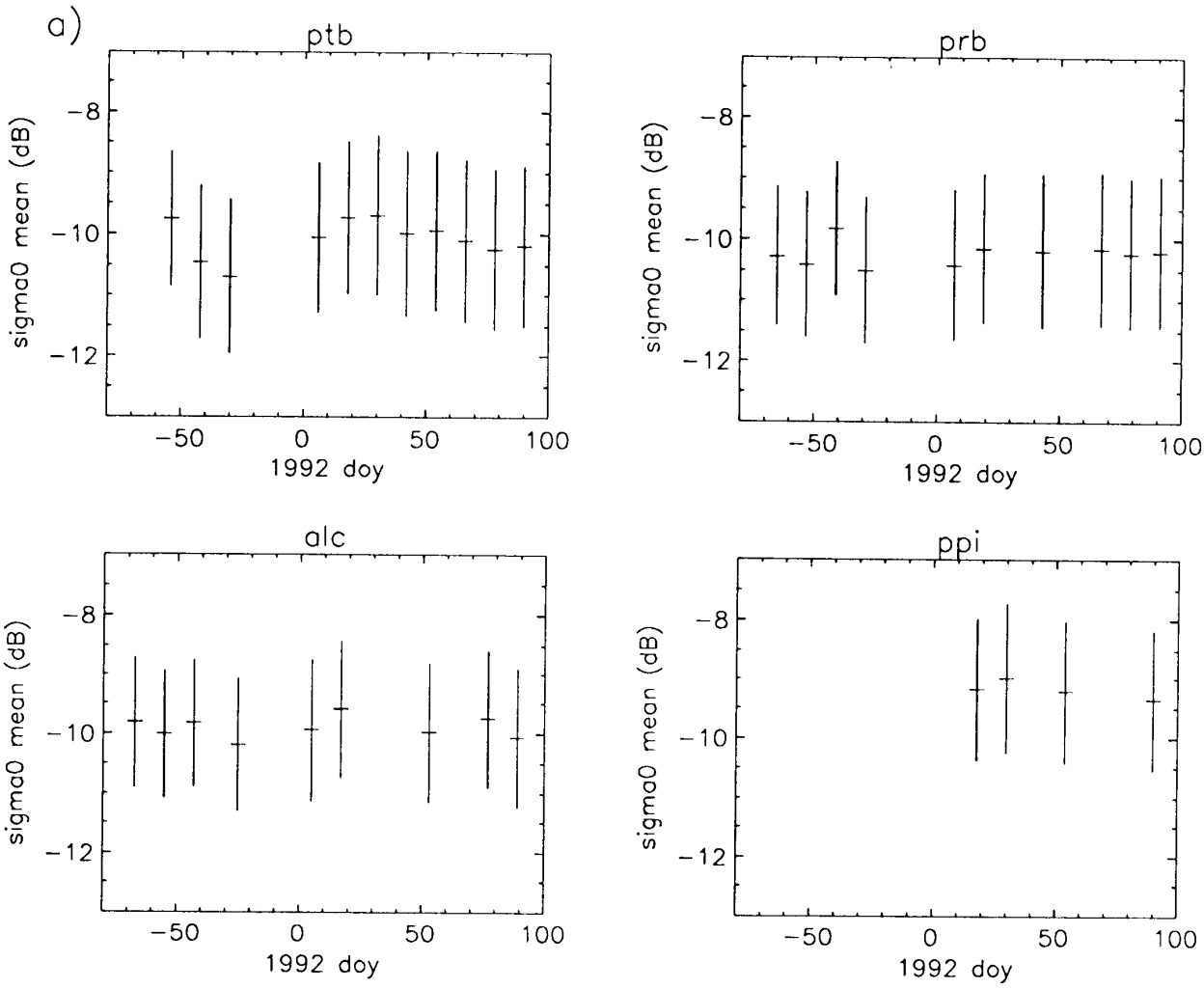
a)
ptb
prb
alc
ppi
sigma0 mean (dB)
-8
-10
-12
-50
0
50
100
1992 doy

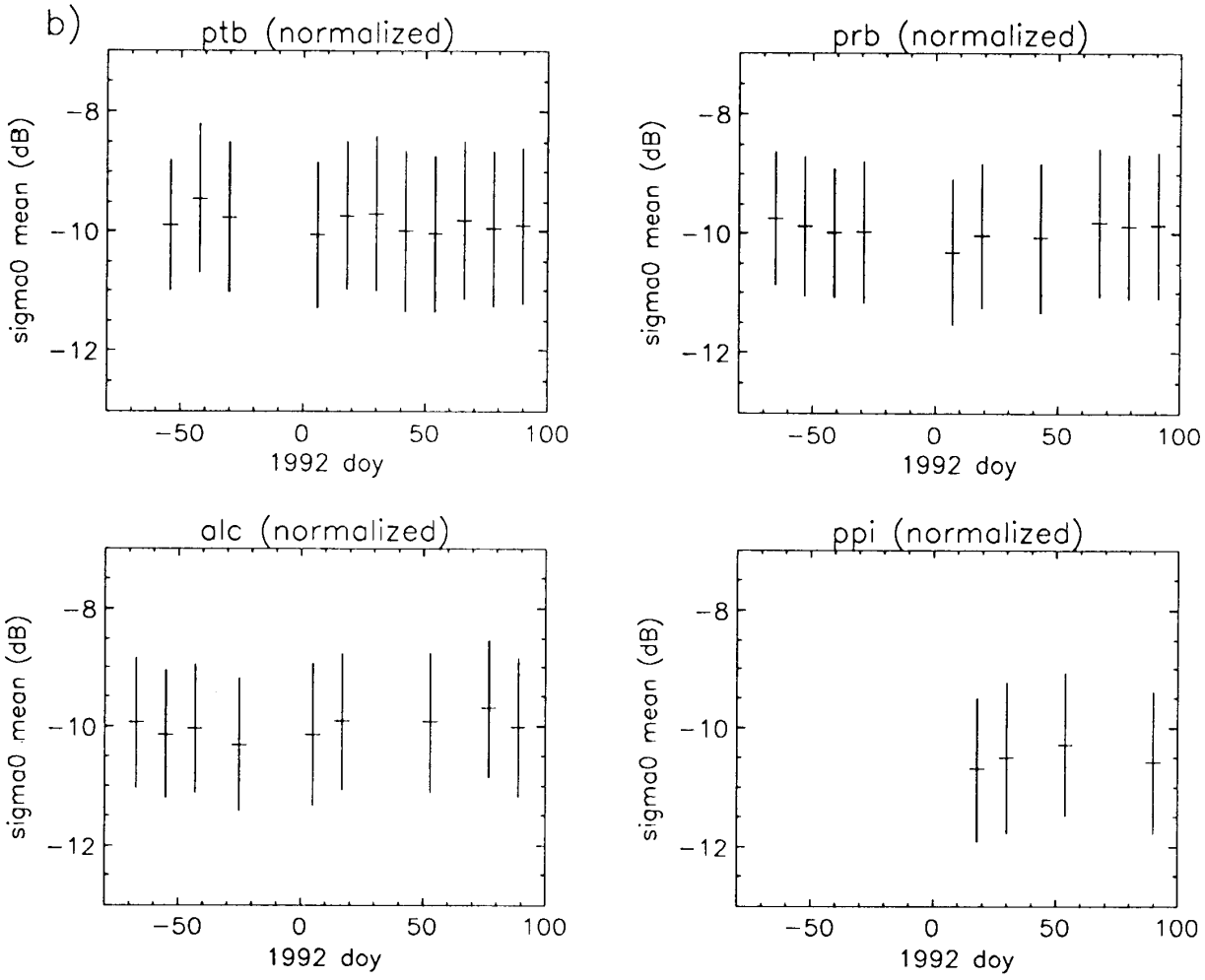
b)
ptb (normalized)
prb (normalized)
alc (normalized)
ppi (normalized)
sigma0 mean (dB)
-8
-10
-12
-50
0
50
100
1992 doy

F. 8

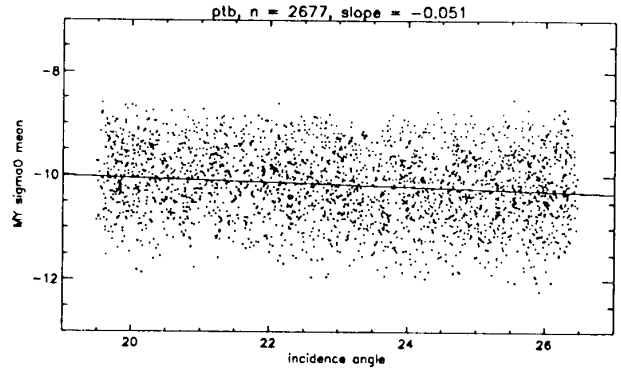
ptb, n = 2677, slope = −0.051
MY sigma0 mean
incidence angle

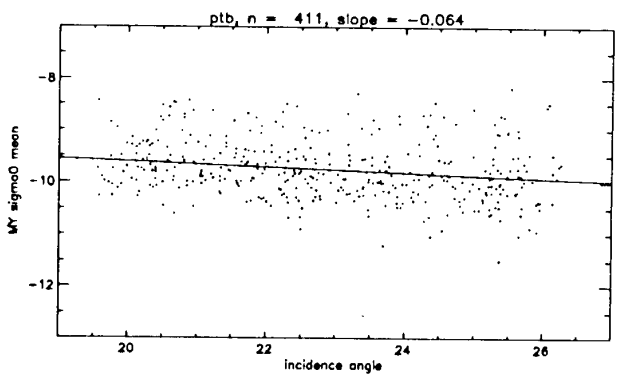
ptb, n = 411, slope = −0.064
MY sigma0 mean
incidence angle

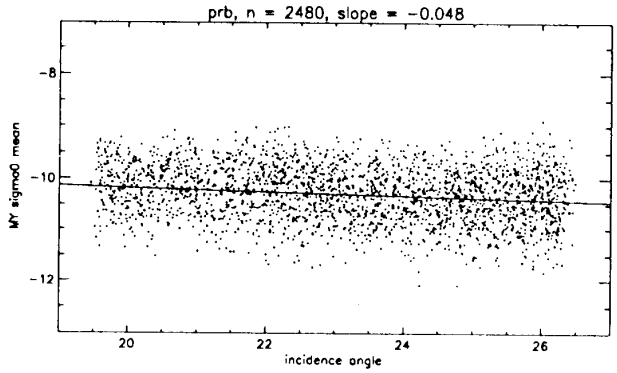
prb, n = 2480, slope = −0.048
MY sigma0 mean
incidence angle

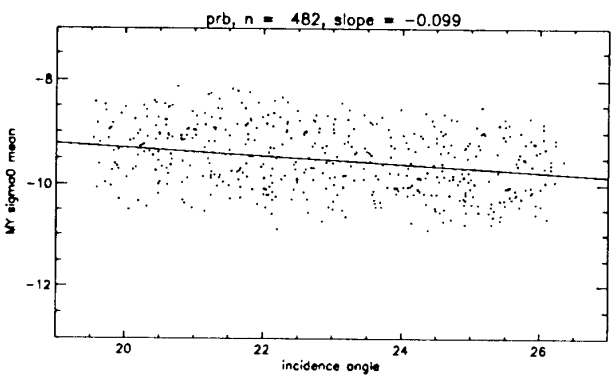
prb, n = 482, slope = −0.099
MY sigma0 mean
incidence angle

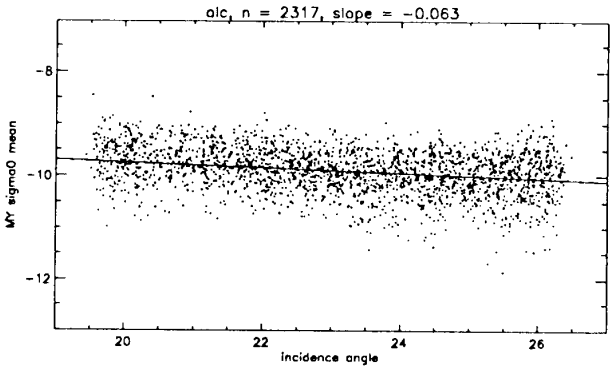
alc, n = 2317, slope = −0.063
MY sigma0 mean
incidence angle

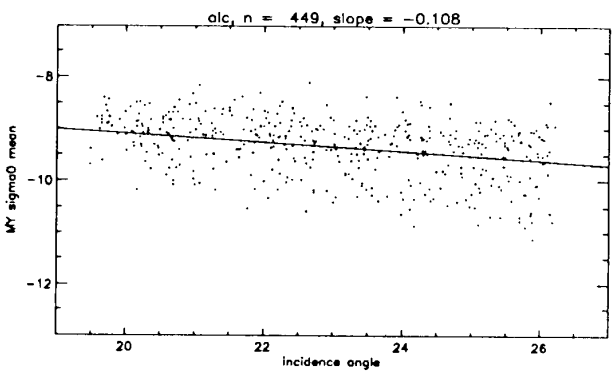
alc, n = 449, slope = −0.108
MY sigma0 mean
incidence angle

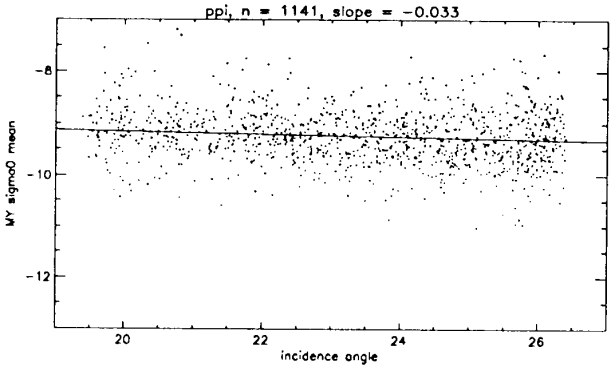
ppi, n = 1141, slope = −0.033
MY sigma0 mean
incidence angle

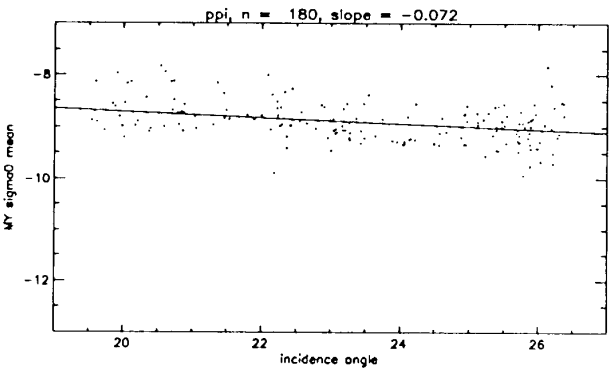
ppi, n = 180, slope = −0.072
MY sigma0 mean
incidence angle

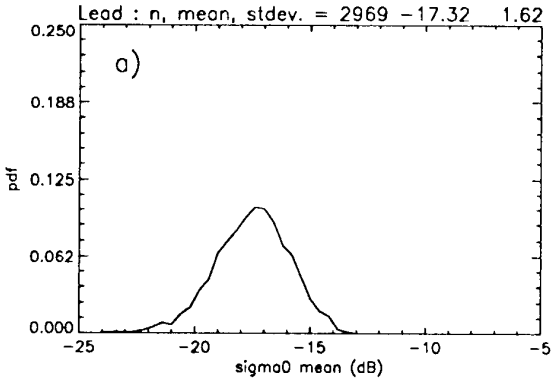
Lead : n, mean, stdev. = 2969 -17.32 1.62
a)
0.250
0.188
0.125
0.062
0.000
pdf
-25
-20
-15
-10
-5
sigma0 mean (dB)

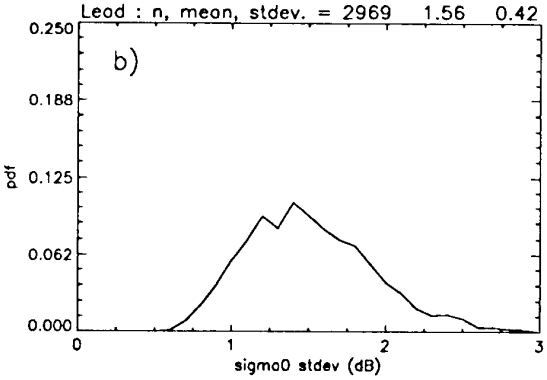
Lead : n, mean, stdev. = 2969 1.56 0.42
b)
0.250
0.188
0.125
0.062
0.000
pdf
0
1
2
3
sigma0 stdev (dB)

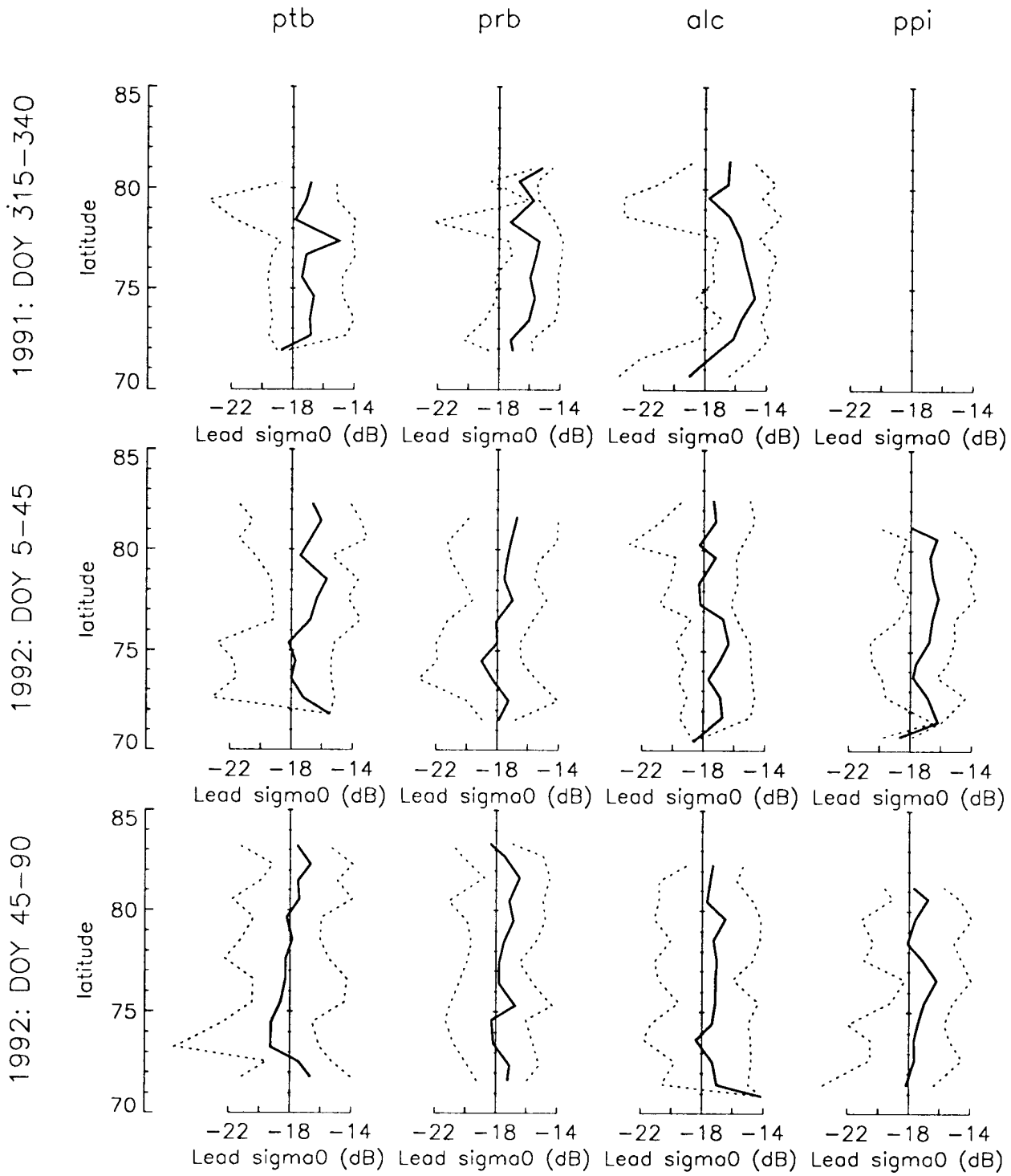
ptb
prb
alc
ppi
1991: DOY 315–340
1992: DOY 5–45
1992: DOY 45–90
latitude
85
80
75
70
−22 −18 −14
Lead sigma0 (dB)

F.11

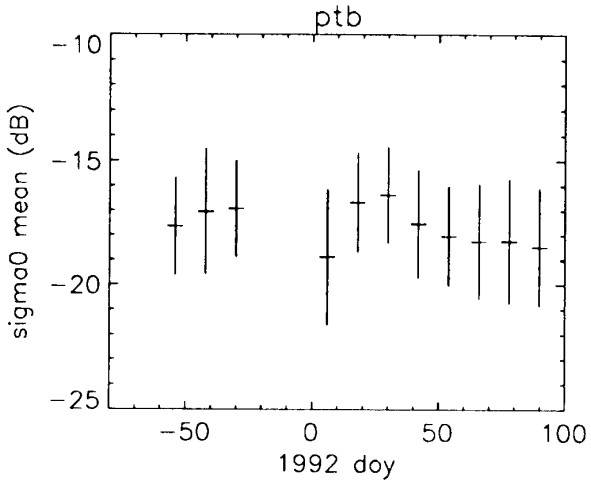
ptb
sigma0 mean (dB)
−10
−15
−20
−25
−50
0
50
100
1992 doy

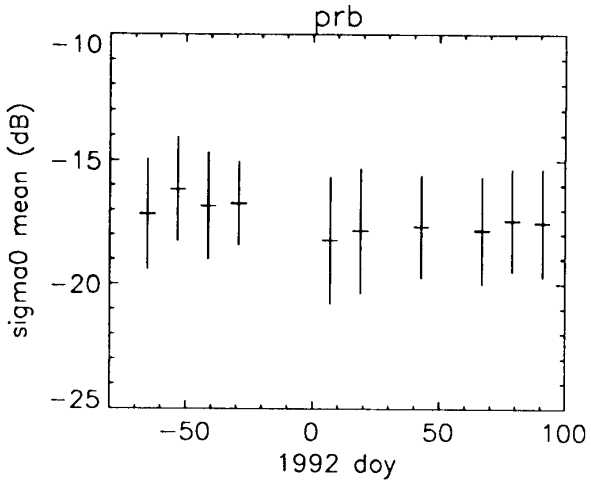
prb
sigma0 mean (dB)
−10
−15
−20
−25
−50
0
50
100
1992 doy

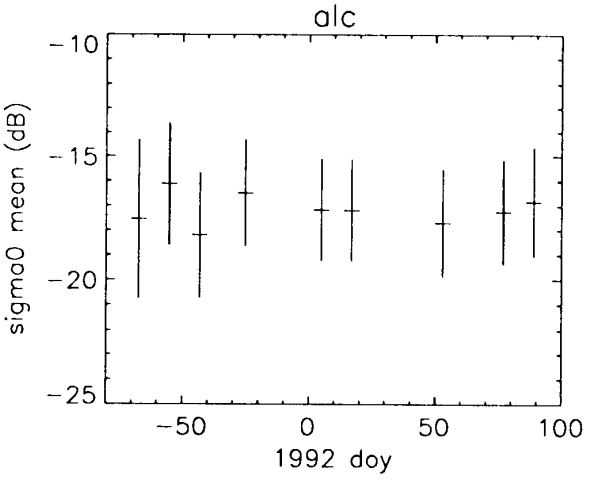
alc
sigma0 mean (dB)
−10
−15
−20
−25
−50
0
50
100
1992 doy

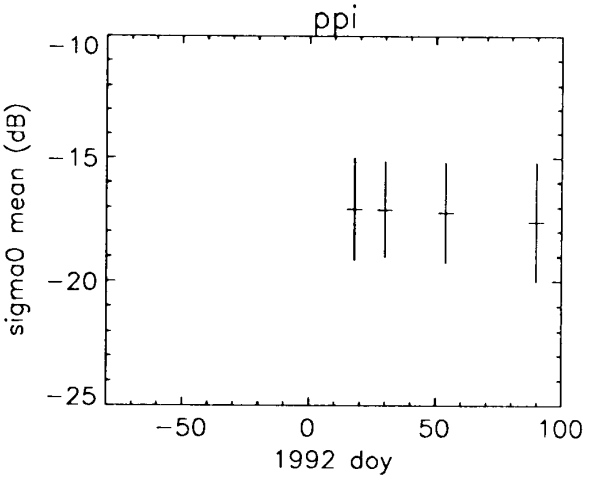
ppi
sigma0 mean (dB)
−10
−15
−20
−25
−50
0
50
100
1992 doy

F.12

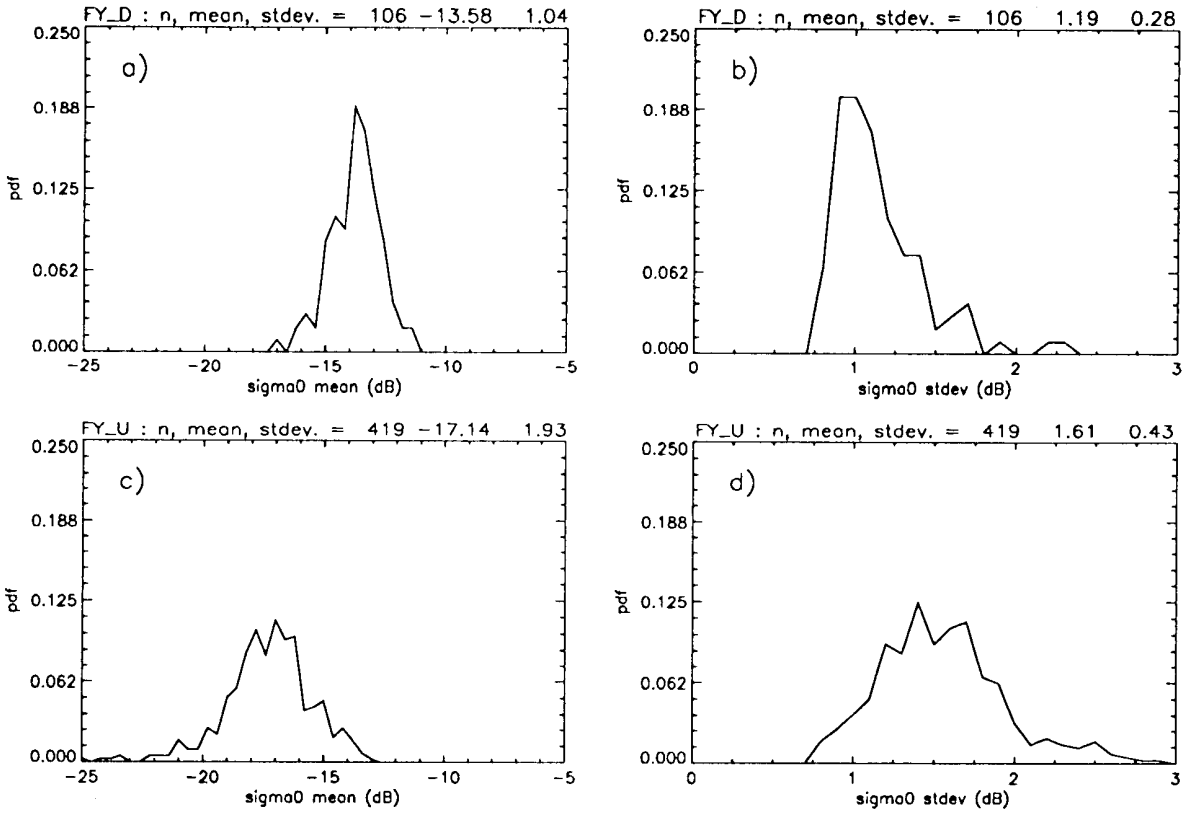
FY_D : n, mean, stdev. = 106 -13.58 1.04
a)
pdf
0.250
0.188
0.125
0.062
0.000
-25
-20
-15
-10
-5
sigma0 mean (dB)
FY_D : n, mean, stdev. = 106 1.19 0.28
b)
pdf
0.250
0.188
0.125
0.062
0.000
0
1
2
3
sigma0 stdev (dB)
FY_U : n, mean, stdev. = 419 -17.14 1.93
c)
pdf
0.250
0.188
0.125
0.062
0.000
-25
-20
-15
-10
-5
sigma0 mean (dB)
FY_U : n, mean, stdev. = 419 1.61 0.43
d)
pdf
0.250
0.188
0.125
0.062
0.000
0
1
2
3
sigma0 stdev (dB)